PHYSICS OF BIREFRINGENT FERMIONS

by

Nazanin Komeilizadeh

B.Sc. (Physics), University of Tehran, 2004

M.Sc. (Physics), University of Windsor, 2007

THESIS SUBMITTED IN PARTIAL FULFILLMENT

OF THE REQUIREMENTS FOR THE DEGREE OF

DOCTOR OF PHILOSOPHY

IN THE

DEPARTMENT OF PHYSICS

FACULTY OF SCIENCE

SIMON FRASER UNIVERSITY

Fall 2012

APPROVAL

Name:	Nazanin Komeilizadeh
Degree:	Doctor of Philosophy
Title of thesis:	Physics of Birefringent fermions
Examining Committee:	Dr. J. Steven Dodge Associate Professor (Chair)
	Dr. Malcolm Kennett, Senior Supervisor Associate Professor
	Dr. Igor Herbut, Supervisor Professor
	Dr. Paul Haljan, Supervisor Associate Professor
	Dr. Jeff McGuirk, Internal Examiner Associate Professor
	Dr. Arun Paramekanti, External Examiner Associate Professor, Department of Physics, University of Toronto
Date Approved:	December 07, 2012

Abstract

There has been much recent interest in Dirac fermions due to their physical realization as low energy excitations in graphene. In this thesis we introduce birefringent relativistic fermions, for which the chiral symmetry usually present for Dirac fermions is broken, and there can be more than one Fermi velocity. We first introduce a lattice model of spinless fermions that can arise from a scheme to introduce an artificial magnetic field for cold atoms. This model has an unusual Hofstadter-like spectrum as a function of the flux per plaquette. When there is an average of half a flux quantum per plaquette, the model has Dirac points in its spectrum and exhibits low energy excitations with two different "speeds of light", i.e. birefringent fermions. We investigate the effects of several perturbations on the spectrum such as staggered potentials and topological defects and we study the ordered phases that can arise from interactions. We find that sufficiently strong nearest neighbour interactions lead to a charge density wave phase but that next-nearest neighbour interactions allow the possibility of other phases. We also study the response of birefringent fermions to a magnetic field and discuss how both Landau levels and the Integer Quantum Hall effect for regular Dirac fermions are modified for birefringent fermions.

To Mom, Dad, Yasamin and my dear Saeed

Acknowledgments

First and foremost, I would like to thank Malcolm Kennett for his supervision during my studies at SFU. Thanks to Paul Halijan for kindly accepting to be in my supervisory committee. I would like to also thank George Kirczenow for teaching me physics and patiently answering my questions in his office with his friendly manner that always made me comfortable in asking him the simplest questions that I might have thought to be worthless asking. Moreover, I need to thank Igor for accepting to be in my supervisory committee when I was half way through my degree. I cannot thank Igor enough for his all-time helpful discussions both in class and in his office. Besides our physics discussions, I very much enjoyed talking to Igor about philosophy and life in general. I sincerely find myself fortunate that I was given this opportunity to get to know his great personality and it is my real honor to call him a friend and I hope I can keep this friendship for many more years. He was the only person in the physics department that influenced my life in many ways and motivated me to keep up with my goals and has always been a kind and reliable person to be stood by and his advice has been and will be with me forever.

So many other people apart from my immediate family helped me throughout this thesis. I need to give thanks to the physics people in our department and outside of our physics department, especially, Payam Mousavi, Sara Sadeghi, David Lee, Bitan Roy, Peter Smith, Kelly Cheung, Saeed Falahat, Alireza Hojjati, Sara Ejtemaee, Fatemeh Rostamzadeh Renani, Yiwei Zhang, Kamran Kaveh, Farnaz Rashidi, Hosein Amooshahi and Zahra Lotfi who have helped me in one way or another throughout my research project. Thanks to the secretaries in the physics department who always kept me updated with the deadlines and prepared me the necessary documentations so I would be able to continue registering at the physics department as an international student.

I would like to express my sincere gratitude to my parents and my sister for their un-

conditional moral support not only during my PhD studies, but also throughout my entire academic journey and for supporting me achieve my goals in life. Thanks Mom, Dad and Yasamin!

Last but definitely not least, my biggest thanks go to the love of my life, my beloved partner Saeed, whom I love more than I love myself. His constant support and love have helped me stand strong and stay focused on my goals and has helped me keep my goals alive during all these years of being together and no words can possibly be able to express my gratitude for having him in my life. I specially need to thank him for the beautiful peaceful heaven he has built for me and his everlasting love and support. Without his presence, the writing of this thesis and finishing up the work would have been much harder if not impossible. Thank you my dearest for all these years of support and sheer love and I love you more than anyone can possibly imagine!

Contents

List of Figures

Chapter 1

Introduction

The idea that particles with integer spin condense into a single quantum state at sufficiently low temperatures was first discussed by Satyendra Nath Bose in 1924 and then extended by Albert Einstein [1, 2]. The first experimental realization of Bose-Einstein condensation took place in 1995 [3], utilizing a gas of rubidium atoms cooled to several hundred nanokelvin at the University of Colorado JILA-NIST lab. The cooling of fermions to the quantum degenerate limit followed the work on bosons [4, 5, 6]. These achievements ushered in the field of quantum degenerate cold atoms and Eric Cornell, Carl Wieman and Wolfgang Ketterle were awarded the 2001 Nobel Prize in Physics for their work on Bose-Einstein condensation.

Optical lattices are light-induced periodic potentials which can be used to trap atoms in a spatially regular array. The idea of combining a quantum degenerate gas with the periodic potential of an optical lattice was developed during the 1990s [7, 8, 9, 10]. Atoms trapped in optical lattices represent a system in some sense analogous to condensed matter systems in the sense that quantum particles reside on a spatially periodic lattice. Hence, there has been much interest in ultracold atoms in optical lattices from the condensed matter community. Once experimental techniques were established, a number of theoretical papers were published predicting physics that might be observed in such systems (see Ref. [10] and references therein), making use of analogies between cold atoms in an optical lattice and condensed matter systems to suggest the simulation of phenomena that are not realized in condensed matter settings, e.g. bosonic quantum Hall effects. In order to simulate the phenomenon of the quantum Hall effect, which usually occurs when there is a strong

magnetic field, the neutrality of atoms requires that any gauge fields generated be artificial. This has led to many suggestions of schemes to generate such fields, which are reviewed in Sec.1.2. Another area of activity is the idea of simulating Dirac fermions, which have been the focus of much recent interest following the discovery of graphene [11], with the goal of making use of the versatility of optical lattices to manipulate the properties of these excitations.

1.1 Cold Atoms in Optical Lattices

Ultracold atoms in optical lattices provide model systems to investigate strongly interacting quantum many-body physics through quantum simulation as proposed by Feynman [12, 13]. Other possible applications include quantum computing and quantum information processing as the weak interactions between the neutral atoms in the ultracold atoms in an optical lattice and the environment lead to long coherence times [14]. An experimental advantage of using optical lattices is that it is possible to control the parameters of the system, such as lattice depth and the interactions between particles with both high precision and tunability [10].

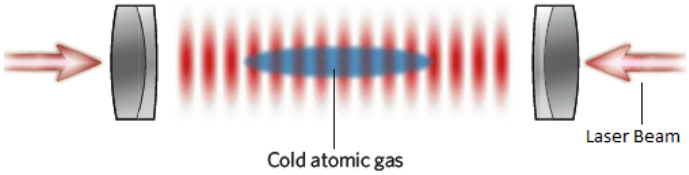

Figure 1.1: Formation of a one-dimensional optical lattice by superimposing two travelling waves [15]. Copyright 2008 by Nature.

Cold atoms can be cooled and consequently be trapped in optical lattices that are generated by superpositions of laser beams (illustrated for one-dimension in Fig. 1.1) [16]. The first step is to trap the atoms in a harmonic magnetic trap and then the optical lattice is imposed on top of the harmonic trap. The optical lattice arises from the standing wave due to the interference between two counterpropagating laser beams. Such a construction can be generalized to two dimensions via overlapping two optical standing waves along

orthogonal directions to create a square lattice potential, as shown in Fig. 1.2.

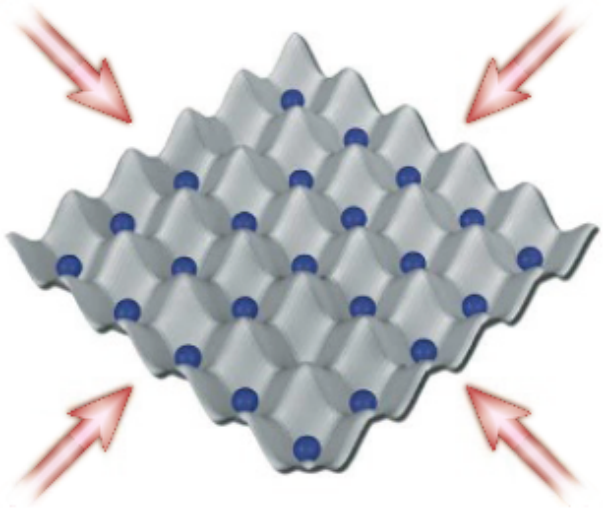

Figure 1.2: Two-dimensional optical lattice formed by superposition of two standing waves [15]. Copyright 2008 by Nature.

For more complicated lattices or higher dimensions, additional lasers are required. The main focus in this thesis will be two dimensional square lattices.

The physical basis for the confinement of cold atoms in an optical lattice is the dipole force [17]:

$$\vec{F} = \frac{1}{2}\alpha(\omega_L)\vec{\nabla}\left[|\vec{E}(\vec{r})|^2\right], \tag{1.1}$$

where $|\vec{E}(\vec{r})|^2$ the time-averaged intensity of the electric field associated with the laser beams and $\alpha(\omega_L)$ is the polarizability of the atoms at the laser frequency ω_L. The time-average of the intensity enters Eq. (1.1) provided that the time scale for the motion of the center-of-mass of the atoms is much larger than the inverse frequency of the laser beam ω_L^{-1} [17]. Moreover, the sign of the polarizability $\alpha(\omega_L)$ dictates the direction of the force. In the vicinity of an atomic resonance, the form of the polarizability is given by $\alpha(\omega_L) \approx |\langle e|\hat{d}_{\vec{E}}|g\rangle|^2/\hbar(\omega_0 - \omega_L)$, where ω_0 is the transition frequency and $\hat{d}_{\vec{E}}$ the dipole operator in the direction of the field and the ground and excited states are denoted by $|g\rangle$ and $|e\rangle$, respectively [17]. As one can see, Eq. (1.1) shows that depending on the sign of the polarizability, the dipole force guides the atoms either towards nodes or antinodes of

the intensity profile. Thus, one can use this property to locate the neutral atoms at specific points in a spatially varying intensity profile $I(\vec{r})$[17]. The optical lattice potential for a square lattice in two dimensions is of the form:

$$V(x,y) = V_0 \left[\cos^2(k_x x) + \cos^2(k_y y)\right].$$

Due to quantum tunneling, atoms can move in an optical lattice even if the well depth of the lattice is higher than the energy of the atoms. By increasing the depth of the optical potential, the atomic wave function becomes more localized and consequently the on-site interaction increases. The trap depth is linearly proportional to the laser power and typically ranges from a few kHz up to 1 MHz (from the nanokelvin to the microkelvin regime) [17]. The many-body Hamiltonian for N interacting fermions, for the case of cold atoms, in the presence of a trapping potential, $V_{\text{ext}} \neq 0$, in three dimensions is given by [10]:

$$\hat{H} = \int d^3x \psi^\dagger_\sigma(\vec{x}) \left[-\frac{\hbar^2}{2m}\nabla^2 + V_{\text{ext}}\right] \psi_\sigma(\vec{x}) + \frac{1}{2}\frac{4\pi a_s \hbar^2}{m} \int d^3x \psi^\dagger_\sigma(\vec{x}) \psi^\dagger_{\sigma'}(\vec{x}) \psi_{\sigma'}(\vec{x}) \psi_\sigma(\vec{x}),$$

where $\psi_\sigma(\vec{x})$ denotes a field operator for a fermion in a given internal atomic state [10] with spin $\sigma^{(\prime)} = \uparrow, (\downarrow)$ and a_s represents the p-wave scattering length.

In the regime of deep periodic potentials where the energy width of each band in the lattice is much smaller than the gaps between energies of two consecutive bands, it is possible to give a description of the properties of the atoms in terms of a tight-binding model. This leads to the Bose-Hubbard model for bosons or the fermionic-Hubbard model for fermions. The general form of the fermionic Hubbard model is:

$$\hat{H} = -J \sum_{\langle i,j \rangle} \left(\hat{c}^\dagger_{i\uparrow} \hat{c}_{j\uparrow} + \hat{c}^\dagger_{i\downarrow} \hat{c}_{j\downarrow}\right) + U \sum_i \hat{n}_{i\uparrow} \hat{n}_{i\downarrow},$$

where $\langle i,j \rangle$ indicates nearest neighbour sites on the lattice and $\hat{c}^\dagger_{i\sigma}(\hat{c}_{j\sigma})$ represents the fermionic creation (annihilation) operator of particles with spin $\sigma = \uparrow, \downarrow$. The hopping energy from one site to the other through the wells in the optical lattice is given by [10]:

$$J \approx -\int d^3x \left[\frac{\hbar^2}{2m} \nabla\phi_{n,\sigma} \cdot \nabla\phi_{n+1,\sigma} + \phi_{n,\sigma} V_{\text{ext}} \phi_{n+1,\sigma}\right],$$

where the $\phi_{n,\sigma}$s are the Wannier functions that are localized wavefunctions in the n^{th} potential minimum [10]. The Bloch functions, $\psi_{n,\vec{q},\sigma}(\vec{r})$ are connected to the Wannier functions,

$\phi_{n,\vec{R},\sigma}(\vec{r})$, via the Fourier transform on the lattice [17]:

$$\psi_{n,\vec{q},\sigma}(\vec{r}) = \sum_{\vec{R}} \phi_{n,\vec{R},\sigma}(\vec{r}) e^{i\vec{q}.\vec{R}},$$

where $\vec{R}$ is the position the Wannier function is centred on. Since the Wannier functions have an orthonormality relation for all bands n and sites $\vec{R}$, they form a complete orthogonal basis. Therefore, one may expand any operator in terms of the complete basis of Wannier states. On the other hand, the on-site interaction energy per fermion on a single lattice site for a given condensate wavefunction can be written as [10]:

$$U = g \int d^3x \, |\phi_n(\vec{x})|^4,$$

with $g = \dfrac{4\pi\hbar^2 a_s}{m}$ [10] where a_s represents the p-wave scattering length. As it is stated, cold atoms can be trapped in optical lattices generated by laser beams, therefore, the ratio of the on-site energy to the hopping energy can be varied by changing the intensity of the optical lattice [16, 18, 19]. In the limit where the amplitude of the trapping potential of the lattice V_0 is much larger than the recoil energy $E_r = \hbar^2 k^2/2m$, namely $V_0 \gg E_r$, the tunneling energy may be expressed by [17]:

$$J \approx \frac{4}{\sqrt{\pi}} E_r \left(\frac{V_0}{E_r}\right)^{3/4} \exp\left[-2\left(\frac{V_0}{E_r}\right)^{1/2}\right],$$

and the on-site interaction energy reads as follows [17]:

$$U = \sqrt{8/\pi} k a_s E_r (V_0/E_r)^{3/4}.$$

1.2 Artificial Magnetic Fields in Cold Atom Systems

Confining electrons in two dimensions in a strong magnetic field results in some fascinating phenomena such as the integer and fractional quantum Hall effects. To date, the integer and fractional quantum Hall effects have only been observed in fermionic systems: two-dimensional electron gases (2DEGs), graphene and layered organic conductors [20]. An opportunity suggested by cold atoms is the possibility of realizing the quantum Hall effects for bosons as well as for fermions. The exploration of such effects with cold atoms

is complicated by the fact that atoms are electrically neutral and do not couple directly to an applied magnetic field. This implies that any simulation of bosonic quantum Hall states requires an artificial rather than a physical magnetic field. The artificial magnetic field can be generated with or without a lattice and is achieved by ensuring that atoms aquire a phase as they go around a closed path [21, 22]. Despite numerous proposals for schemes to realize the integer quantum Hall effect (IQHE) and the fractional quantum Hall effect (FQHE) for bosons [21], this has not yet been achieved experimentally.

Cold atoms offer the advantage of allowing access to other phenomena that are unreachable in condensed matter systems. To achieve a sufficiently large flux per plaquette in a two dimensional electronic system to obtain a Hofstadter Butterfly spectrum, an experimentally unreachable magnetic field on the order of 10^5 T is required. However, an equivalent flux is within reach in cold atom systems [22, 38]. This has led to suggestions for schemes to generate artificial gauge fields that couple to atoms in the same way as a magnetic field couples to charged particles [21, 23, 24, 22, 25, 26, 27, 28, 29, 31, 33, 36]. Among the proposals [21, 23, 24, 22, 25, 26, 27, 28, 29, 31] to couple atoms to an artificial magnetic field, several have been implemented experimentally [33, 36, 38].

The idea behind all the schemes that have been suggested to generate an artificial magnetic field on a lattice is that the motion of particles can be described with a tight-binding model where there is hopping between spatially localized single-particle states, represented mathematically by elements in a hopping matrix. As a result, the magnetic field is realized by the phase that is accumulated by the particle as it hops in a closed loop around a plaquette on the lattice. The phase aquired by each element of the hopping matrix is known as the Peierls phase [39]. The strength of the magnetic field in a lattice system can be measured in terms of the magnetic flux through each plaquette. For a particle of a given charge e, the phase aquired when the particle hops around a plaquette is $2\pi e\phi/h = 2\pi\phi/\phi_0$, where $\phi_0 = h/e$ is the flux quantum. This is illustrated in Fig 1.3.

The following subsections are devoted to introducing several proposals for methods with which magnetic fields in neutral atoms can be generated with discussion of current experimental results. Specifically, we first introduce rotating systems in which an artificial magnetic field is created in a system composed of a rapidly rotating cloud of degenerate neutral cold atoms. Second, we present the method of time-varying quadrupole potential where the artificial magnetic field is achieved through a time-dependent quadrupolar po-

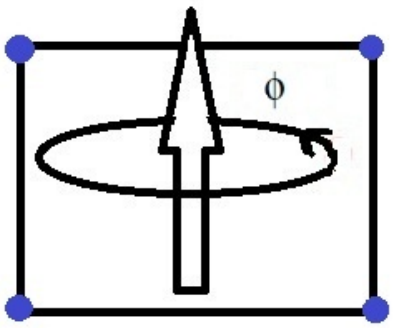

Figure 1.3: Schematic picture of a magnetic flux, ϕ, that goes through a plaquette.

tential applied in conjunction with modulation of nearest neighbour hopping as a function of time. Third, we discuss Raman-assisted tunnelling in which two Raman lasers are used in optical lattices to create an artificial magnetic field. Finally, we introduce the optical flux lattices method where a particular laser configuration enables one to obtain an effective magnetic field in an optical lattice.

1.2.1 Rotating Systems

One of the first suggestions for achieving artificial magnetic fields for cold atoms was to rotate a Bose-Einstein condensate [36, 40, 41]. The generation of a Bose-Einstein condensate in ultracold atomic gases in experiment is either through the condensation of atomic bosons [42, 43], or fermionic pairs [17]. In the case of neutral atoms in a rotating atomic system, where a lattice is not involved, although the charge neutrality gives rise to no Lorentz force acting on the particles, an equivalent effect can be provided by the Coriolis force. For a particle with velocity $\vec{v}$ the Coriolis force, $\vec{F}_C = 2m\vec{v} \times \vec{\Omega}$, that results in the frame of reference of a rotating system has the same mathematical structure as the Lorentz force, $\vec{F}_L = q\vec{v} \times \vec{B}$, for the case of a charged particle in a magnetic field. The Hamiltonian for N identical interacting neutral particles, such as a system of atomic gas, that are confined in a harmonic trap with natural frequencies $\omega_{\|}$ and $\omega_{\perp}$ and with a symmetric potential about the z axis is

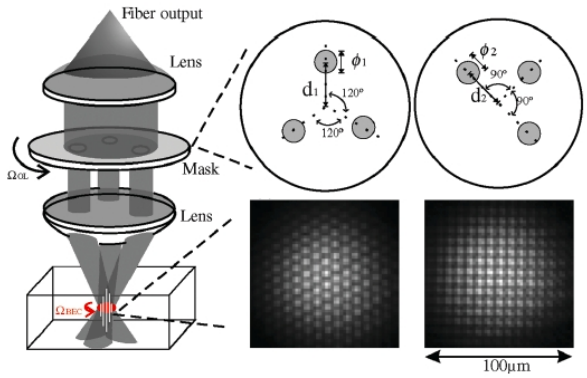

Figure 1.4: Schematic diagram of the rotating optical lattice for a triangular (on the top left) and square (on the top right) optical lattices. Bottom left and bottom right are pictures of vortex lattices on triangular and square optical lattices respectively [40]. Copyright 2006 by the American Physical Society.

given by [23]:

$$\hat{H} = \sum_{i=1}^{N} \left[\frac{|\vec{P}_i|^2}{2M} + \frac{1}{2} M\omega_\perp^2 (x_i^2 + y_i^2) + \frac{1}{2} M\omega_\parallel^2 z_i^2 \right] + \sum_{i<j} V(\vec{r}_i - \vec{r}_j).$$

The Hamiltonian in the rotating frame about the z-axis with an angular frequency $\vec{\Omega} = \Omega\hat{z}$ is given by [23]:

$$H_\Omega = H - \vec{\Omega} \cdot \vec{L},$$

where the one-body term can be simplified to [23]:

$$H_\Omega^{(1)} = \frac{|\vec{P}_i - M\vec{\Omega} \times \vec{r}_i|^2}{2M} + \frac{1}{2} M(\omega_\perp^2 - \Omega^2)(x_i^2 + y_i^2) + \frac{1}{2} M\omega_\parallel^2 z_i^2.$$

The kinetic energy term has exactly the same mathematical structure as for a particle moving in a uniform magnetic field aligned along the z-direction. Experimentally, applying a rotation to a Bose-Einstein Condensate gives rise to the observation of quantized vortices [17, 37, 44, 45].

In the lattice case, one experimental set-up is such that the initial state is a non-rotating condensate in a static lattice. The lattice is then rotated at an increasing rate, generating a rotating system where one is able to create an effective magnetic field as above. The

authors of Refs. [40] and [41] did an experimental study of rotating optical lattices on a sample of ^{87}Rb kept in a Bose condensed phase. The rapid rotation of the sample gives rise to the formation of quantized vortices which order themselves into a vortex array. This is illustrated in Fig. 1.4. The experiment was done on both triangular and square optical lattices with large lattice spacing in order to lower the strength of interparticle interactions.

The downside of the method of rotating ultracold atoms is that the strength of the artificial magnetic field is limited by instabilities that result from the centrifugal force. This is due to the fact that once the rotation frequency and the frequency of the atomic trap equal each other, the trapping is cancelled by the centrifugal force that is present in the rotating frame [46]. Another problem is from heating; in the laboratory frame, any static perturbation whose wavelength is less than that of the order of the radius of the rotating cloud can cause heating as it can excite collective modes of the rotating gas [23]. Additionally, in order to use rotations, the cold atom system must be held in a trap with axial symmetry. This limits the experimental configurations that may be used, and suggests that alternative methods for generating an artificial magnetic field rather than rotation may be desirable.

1.2.2 Time-varying Quadrupole Potential

Sørensen *et al.* suggested a scheme to create an artificial magnetic field on a lattice by using a combination of modulation of hopping in time in the presence of a time-varying quadrupole potential. The scheme suggested in Ref. [21] requires two steps to generate an artificial magnetic field. First, a time-varying quadrupolar potential $V(t) = V_{qp}\sin(\omega t)\hat{x}\hat{y}$ ($\hat{x}$ and $\hat{y}$ are position operators) is applied to the system and second, the hopping is modulated as a function of time. During the course of one oscillation of the quadrupolar potential, hopping in the x-direction is turned on for a very short period of time $\tau \ll t_0 = \frac{2\pi}{\omega}$ at times $t = nt_0$, where n is an integer, and hopping in the y-direction is turned on for time τ around $t = \left(n+\frac{1}{2}\right)t_0$. The time dependence of the hopping and the potential are illustrated in Fig. 1.5, and the mechanism by which flux is introduced is illustrated in Fig. 1.6.

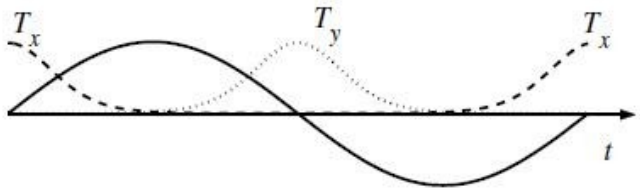

Figure 1.5: Modulation of the hopping in the x and y directions as a function of time during the course of one period that creates an effective magnetic field [21]. Copyright 2005 by the American Physical Society.

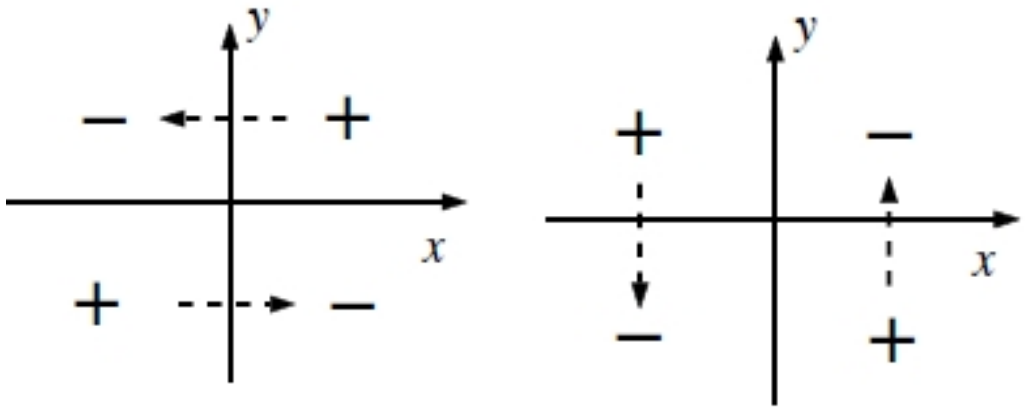

Figure 1.6: Tunneling in the x- (on the left) and y- (on the right) directions is followed by a positive potential in the first and third quadrant (on the left) and second and fourth (on the right), and hence atoms will experience a lower potential by moving in the direction of the dashed arrows. When the dashed arrows are combined together, they make a circular cyclotron motion [21]. Copyright 2005 by the American Physical Society.

Due to the periodic oscillation in the Hamiltonian, the time evolution operator after m periods may be written as $U(t = mt_0) = U(t = t_0)^m$. An effective Hamiltonian describing the time evolution results [21]:

$$H_{\text{eff}} \approx -J \sum_{x,y} \left[c^{\dagger}_{x+1,y} c_{x,y} + c^{\dagger}_{x,y+1} c_{x,y} e^{i2\pi\alpha x} + \text{h.c} \right],$$

where the parameter $\alpha = V_{qp}/\pi\hbar\omega$ acts as an effective magnetic flux and the effective tunneling strength is represented by J. We give more details about this scheme and consider a particular modification in Chapter 2.

1.2.3 Raman-Assisted Tunneling

The idea of using Raman-assisted tunnelling to generate an artificial magnetic field was suggested by Jaksch and Zoller [22]. In the simplest scheme to implement this proposal, two Raman lasers are used to transfer atoms from one state to another and to make them hop between different sites. The means by which one generates a non-zero flux through plaquettes of a lattice is illustrated in Fig. 1.7.

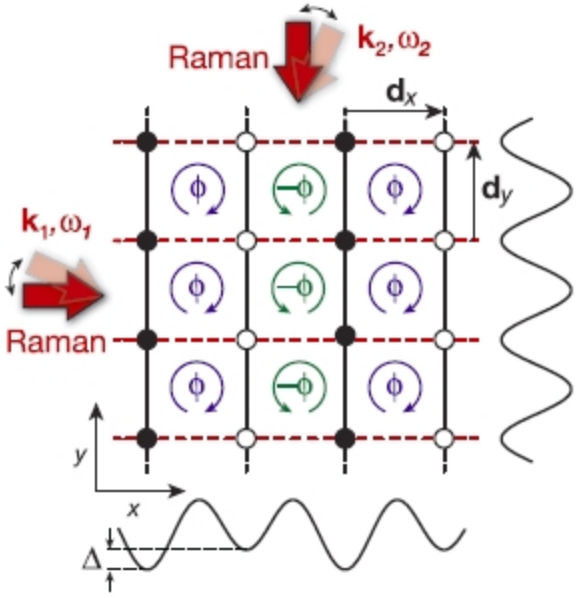

Figure 1.7: A pair of Raman lasers with wave vectors $\vec{k}_{1,2}$ and frequency difference $\omega_1 - \omega_2 = \Delta/\hbar$, with Δ the amplitude of the staggered potential offset, give rise to an effective flux $\pm\phi$ per plaquette with alternating sign along the x-direction [38]. The black and white dots refer to two different internal states of the atoms. Copyright 2011 by the American Physical Society.

The mathematical description of the experimental setup is similar to the Hamiltonian of a system of charged particles hopping on a lattice that are subjected to an external perpendicular magnetic field [38]:

$$\hat{H} = -\sum_{\vec{R}} (K(\vec{R}) a^{\dagger}_{\vec{R}} a_{\vec{R}+\vec{d}_x} + J a^{\dagger}_{\vec{R}} a_{\vec{R}+\vec{d}_y}) + \text{H.c.},$$

where $\vec{d}_x$ and $\vec{d}_y$ are the lattice spacings in the x and y directions and J and $K(\vec{R})$ are the hopping integral and Raman-induced hopping integral respectively [38]. Non-vanishing flux is induced in the lattice by adjusting laser parameters, e.g. choosing different wavelengths for the Raman lasers or using different angles between the two laser beams, and results in a nontrivial phase that atoms acquire when they hop around a closed path.

The authors of Ref. [22] showed that the experimental setup of Raman-assisted tunneling might be used to realize the fractal energy bands of the Hofstadter butterfly, which, as noted earlier, is out of reach for electrons in condensed matter systems. Another advantage of using Raman-assisted tunneling compared to condensed matter systems is that the parameters entering the Hamiltonian can be controlled and varied more conveniently and over a wider range [22]. This method has very recently been implemented by Aidelsburger *et al.* [38] to generate effective magnetic flux per four-site plaquette of π and $-\pi$, alternating along the x-direction (Fig. 1.7). Fig. 1.8 shows the experimental realization of the scheme and the good agreement between the theoretical curve and the data from experiment.

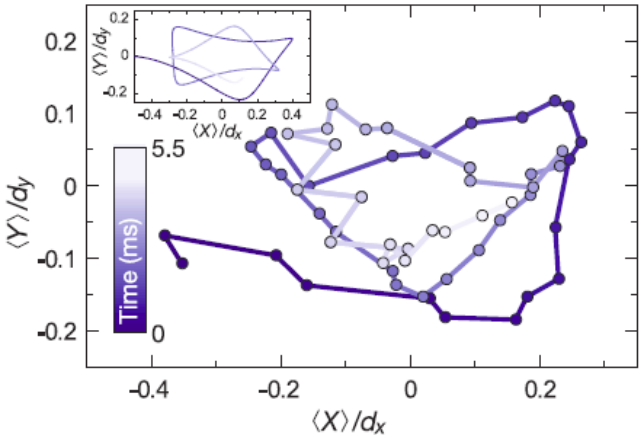

Figure 1.8: Cyclotron orbits of the average particle position that is obtained from the mean atom positions [38]. Copyright 2011 by the American Physical Society.

The simplest version of this method has the drawback that the flux between the neighbouring sites alternates, hence, one cannot maintain a uniform magnetic field through the lattice. Proposals to rectify this are given in Ref. [22].

1.2.4 Optical Flux Lattices

A very recent suggestion as to how to induce artificial magnetic fields for trapped atoms is the use of optical flux lattices [47]. The basis of this idea is that one can generate an effective magnetic field through the adiabatic movement of optically dressed atoms through space in the presence of an appropriate optical potential.

The Hamiltonian for this method describes an atom with two available levels moving in optical fields within the rotating wave approximation [47]:

$$\hat{H} = \frac{\hat{P}^2}{2m}\hat{I} + V\hat{M}(\vec{r}),$$

with $\hat{I}$ the identity matrix, V the energy of the optical potential and $\hat{M}(\vec{r})$ a 2×2 matrix which may be written as $\hat{M} = \vec{M}(\vec{r}) \cdot \vec{\sigma}$ [47]. One of the advantages of this method is that optical flux lattices can be implimented easily as they require a small number of lasers in their setups [47]. Moreover, this method may make the realization of the fractional quantum Hall effect of bosons possible. The reason for this is that this method has the potential to lead to much higher mean flux densities than other proposals [47].

1.3 Dirac Fermions in Condensed Matter and Optical Lattices

The two-dimensional carbon allotrope, graphene, which is a single one-atom-thick sheet of carbon atoms arranged in a honeycomb lattice, was fabricated and investigated by Andre Geim and Kostya Novoselov, for which they received the 2010 Nobel Prize in Physics. The low energy excitations in graphene may be described as Dirac fermions due to the relativistic form of their dispersion and they arise due to the symmetries of the lattice. The band structure of graphene, illustrated in Fig. 1.9, has 6 Dirac points located at the edge of the Brillouin zone; of these six points, only two are inequivalent and are indicated by the

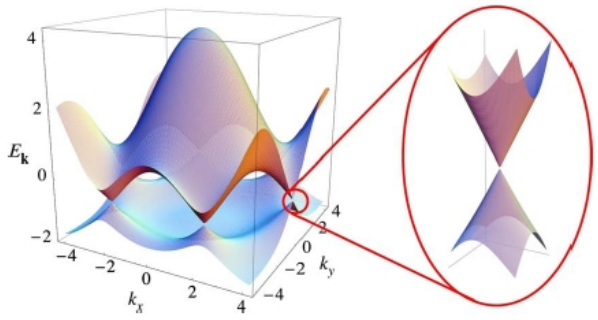

Figure 1.9: Electronic energy dispersion in graphene and close up of one of the Dirac points which shows that the low energy excitations are linear in momentum space [30]. Copyright 2009 by the American Physical Society.

vectors $\vec{K}$ and $\vec{K}'$ in Fig. 1.10. This gives graphene and other systems in which relativistic Dirac fermions are realized unique electrical properties and has made them potential candidates in many applications such as in high mobility, high-frequency transistors and dye-sensitized solar cells [48, 49, 50, 51, 52, 53]. These applications stem from the combination of mechanical properties of graphene such as strength and elasticity, which result from sp^2 hybridized carbon atoms, along with high electronic and thermal conductivities that result from its unique band structure, which is the fact that valence and conduction bands touch each other at the edges of the Brillouin zone and the density of states becomes zero at its Fermi level. Other marvelous properties of graphene also make it a strong candidate for industrial applications [54].

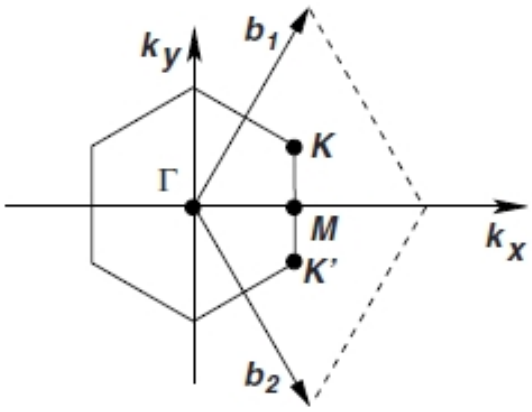

Figure 1.10: Brillouin zone of graphene illustrating the locations of the inequivalent Dirac points K and K' [30]. Copyright 2009 by the American Physical Society.

A number of recent experimental developments and theoretical suggestions indicate that it may be possible to tailor the settings in which Dirac fermions appear and the properties of Dirac cones as a form of "Dirac cone engineering". In particular, two groups have demonstrated Dirac fermions arising in artificial settings [32]. Second, several groups have made suggestions for achieving birefringent Weyl fermions that can have an unusual properties [55]. We review these efforts and proposals below.

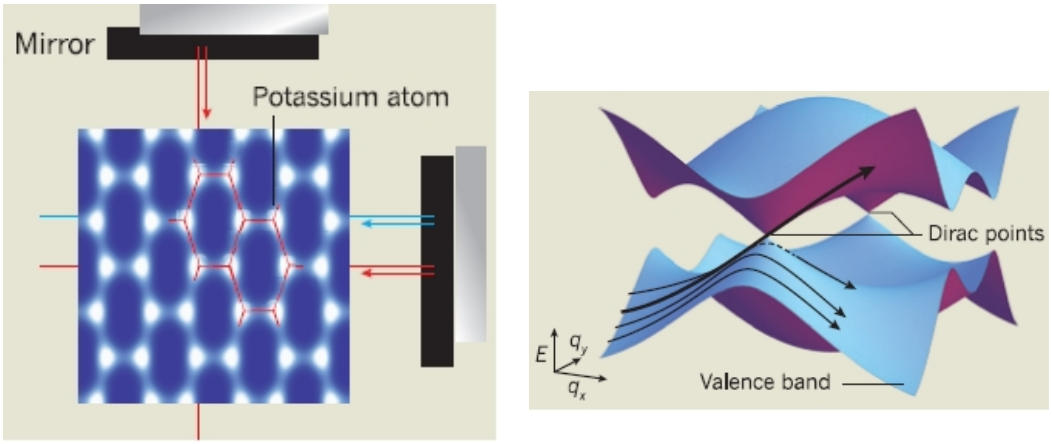

Figure 1.11: Left: Honeycomb optical lattice in which ultracold potassium atoms sit. The arrangement of the lattice is generated via a combination of two interfering laser beams and a separate laser beam. Right: the energy as a function of momentum showing the Dirac points [35]. Copyright 2012 by Nature.

1.3.1 Artificial Dirac Fermions

Besides investigations of systems with a naturally occuring Dirac dispersion relation, recently there has been work to generate Dirac fermions in artificial settings: tunable optical lattices and graphene assembled with an STM tip [32, 34, 35]. In Ref. [32], Tarruell *et al.* studied optical lattices in which they continuously adjusted the geometry to create square, triangular, dimer and honeycomb structures [32], allowing for continuous evolution of the Dirac-like low energy excitations. Figure 1.11 shows the engineering scheme and the Brillouin zone with its associated Dirac point. The position of the Dirac points in the Brillouin zone for the two-dimensional ultracold Fermi gas of potassium atoms were manipulated by varying the lattice anisotropy as is depicted in Fig. 1.12.

1.3.2 Birefringent Weyl Fermions

Lan *et al.* [55, 56] have proposed a scheme for a tight binding model which can be engineered in an optical lattice. In their proposed scheme, the low-energy excitations of the half-filled lattice are described by massless fermions that are described by the following

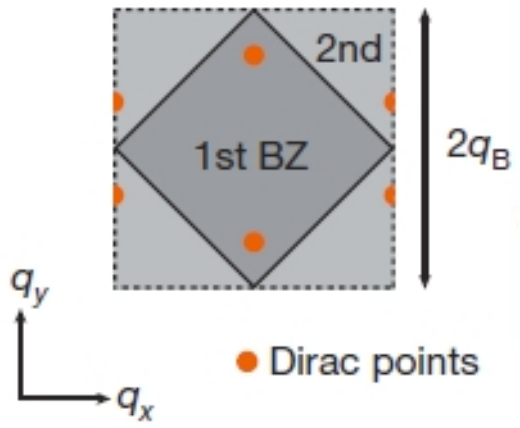

Figure 1.12: First and second Brillouin zones of the tunable honeycomb lattice with adjustable geometry, indicating the positions of the Dirac points [32]. Copyright 2012 by Nature.

Weyl-like Hamiltonian:

$$\hat{H} = v_f \vec{S} \cdot \vec{p},$$

with v_f the Fermi velocity and $\vec{S}$ and $\vec{p}$ spin and momentum operator, respectively. This system shows a semimetallic phase for half odd integer spin and a metallic phase for integer spin, with the metallic phase containing a flat zero-energy band. In the large spin limit, in the semimetal phase, where the spin is half odd-integer, the dispersion can be described as a collection of spin-1/2 species, with each species possessing a different effective speed of light. Therefore, the low-energy excitations are characterized by relativistic spin-1/2 Dirac-Weyl fermions that are propagating at different velocities. A consequence of this would be birefringent Klein tunnelling across a potential barrier [55]. Klein tunneling allows for the penetration of relativistic particles through potential barriers without exponential damping, unlike the case for non-relativistic particles. The schematic overview of Klein tunneling for a spin-3/2 Dirac-Weyl fermion incident on a potential barrier is depicted in Fig. 1.13.

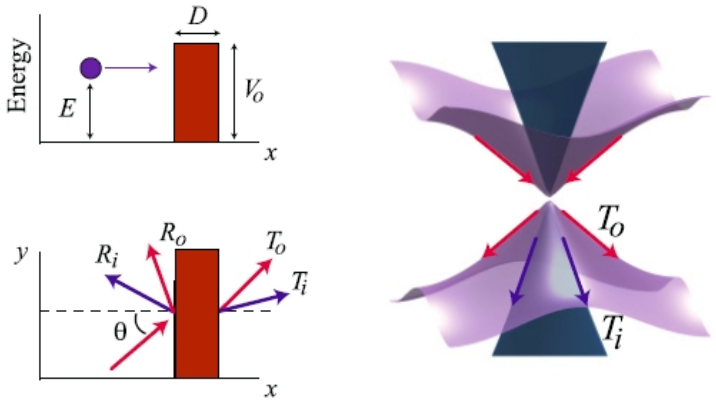

Figure 1.13: Klein tunneling for a spin-3/2 fermion with energy E, barrier width is D and height V_0 that follows the outer cone [55]. Copyright 2011 by the American Physical Society.

1.4 Summary

As discussed in this introduction, cold atoms in optical lattices have the potential for realizing physical situations that have not been achieved in condensed matter systems, either through bosons on a lattice in strong artificial magnetic fields or artificial Dirac fermions. In this thesis we explore themes that follow from the ideas introduced in this Chapter. In Chapter 2, we follow up on the scheme for an artificial magnetic field discussed in Sec.1.2.2 and show how with a small modification, it can lead to an effective lattice model with tunable spatially periodic modulation of the artificial magnetic field and the hopping amplitude and an unusual Hofstadter-like spectrum. In Chapter 3, we study the limit of the tight-binding model that emerges in Chapter 2 when there is an average of half a flux per plaquette and find that the spectrum of low-energy excitations can be described by massless Dirac fermions in which the usually doubly degenerate Dirac cones split into cones with different "speeds of light", which can be tuned to give a single Dirac cone and a flat band.

These gapless birefringent Dirac fermions arise because of broken chiral symmetry in the kinetic energy term of the effective low energy Hamiltonian. We characterize the effects of various perturbations to the low-energy spectrum, including staggered potentials and topological defects. In Chapter 4, we also study the effects of nearest-neighbour and

next-nearest neighbour interactions on a square lattice for birefringent Dirac fermions. In particular, we identify order parameters that can arise in the Hartree-Fock approximation and determine the phase boundaries as a function of the birefringence parameter, β. In Chapter 5, birefringent fermions in magnetic fields are considered. Chapter 6 is devoted to conclusions and future directions. Some of the work in Chapter 2 and 3 has previously been published by the author in collaboration with Malcolm Kennett, Kamran Kaveh and Peter Smith [57].

Chapter 2

Spatially Periodic Artificial Magnetic Fields

In 1976 Douglas Hofstadter predicted that the allowed energy levels of electrons in a two-dimensional square lattice subject to a uniform perpendicular magnetic field have a fractal structure [58]. This fractal structure of eigenvalues as a function of flux per plaquette is the famous Hofstadter butterfly spectrum and is shown in Fig. 2.1. In this chapter, we consider a protocol for inducing an artificial magnetic field for neutral cold atoms that leads to a tight binding Hamiltonian with a tunable Hofstadter-like spectrum. The particular spectrum arises from the combination of hopping and an artificial magnetic field that are both periodically modulated in the x and the y directions. The presence of spatial periodicity in the amplitude as well as the phase of the hopping is the key difference between the model we consider here and previous work on the spectrum of particles in the presence of magnetic fields that are periodic in both the x and y directions [59, 60, 61, 62, 63, 64, 65]. This difference facilitates the unusual Dirac-like excitations that we discuss in Chapters 3 and 4.

As emphasized in Chapter 1, there have been numerous theoretical proposals for schemes to realize artificial magnetic fields with cold atoms, several of which have been implemented experimentally. The particular scheme discussed here may not be as easily implemented as e.g. Raman-assisted tunnelling [38], but the tight-binding model we obtain and its associated physics are independent of the particular choice of scheme used to generate the artificial field.

We first review the proposal of the realization of an artificial magnetic field made by

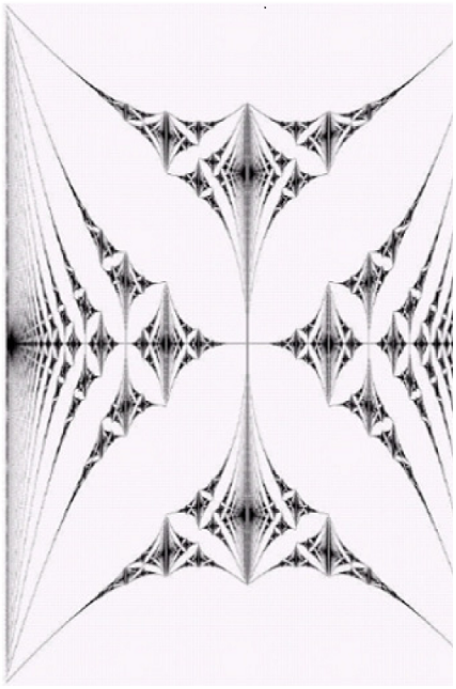

Figure 2.1: The fractal Hofstadter butterfly spectrum. The vertical and horizontal axes represent energy, from $-4J$ to $4J$, and the magnetic flux per plaquette, from 0 to 1, respectively [58]. Copyright 1976 by the American Physical Society.

Sørensen *et al.* [21] in more detail than in Sec.1.2 and then present a modification of Sørensen *et al.*'s proposal. We determine the effective Hamiltonian and the Hofstadter-like spectrum that emerges from this scheme. Most of the material presented in this chapter was published previously in Ref. [57] in collaboration with Malcolm Kennett, Kamran Kaveh and Peter Smith. The author's contribution to this work was in deriving the effective tight-binding model and initial numerical investigations of its spectrum both in the absence and presence of a trap. More extensive numerical results were obtained by Peter Smith and the figures displayed in this chapter were generated by him.

2.1 Realization of an Artificial Magnetic Field

In this section, we further discuss the scheme presented by Sørensen *et al.* [21] and then introduce our modification of their proposal. We then present a series of Hofstadter butterflies one can obtain by changing the tunable parameters of the problem. We end the chapter with a discussion of the effects of trapping potentials that are relevant for cold atom realizations of this physics.

2.1.1 Proposal by Sørensen *et al.*

Sørensen *et al.* [21] proposed a scheme for realizing effective magnetic fields in two-dimensional neutral bosonic cold atom systems in an optical lattice. They proposed modulating the hopping in the x and y directions as a function of time and simultaneously applying a time varying quadrupole potential $V(t) = V_{qp}\sin(\omega t)\hat{x}\hat{y}$. This strategy is shown in Fig. 1.5, where $\hat{T}_{x(y)}$ are hopping operators describing hopping in the $x(y)$ directions respectively. Specifically, hopping in the x direction is turned on for a short time $\tau \ll t_0$ around $t = nt_0$, and tunnelling in the y direction is turned on for a short time τ around $t = (n+\frac{1}{2})t_0$ with $n = 0,1,2,\ldots$, and $t_0 = 2\pi/\omega$. The operators for hopping in the x and y directions are $\hat{T}_x = -\mathcal{J}\sum_{x,y}\left(\hat{c}^\dagger_{x+1,y}\hat{c}_{x,y} + \text{h.c.}\right)$ and $\hat{T}_y = -\mathcal{J}\sum_{x,y}\left(\hat{c}^\dagger_{x,y+1}\hat{c}_{x,y} + \text{h.c.}\right)$, respectively.

The time evolution operator in the Schrodinger picture after m periods of the quadrupolar potential is $\hat{U}(t = mt_0) = [\hat{U}(t = t_0)]^m$, where $\hat{U} = \mathcal{T}\{\exp\left(\frac{-i}{\hbar}\int dt'\hat{H}(t')\right)\}$ ($\mathcal{T}$ is the time ordering operator). To see the procedure in more detail, calculate the time evolution operator during one period t_0 explicitly:

$$\hat{U}(t=t_0) = \exp\left(-\frac{i\tau}{2\hbar}\hat{T}_x\right)\exp\left(\frac{2i}{\omega\hbar}V_{qp}\hat{x}\hat{y}\right)\exp\left(-\frac{i\tau}{\hbar}\hat{T}_y\right)\exp\left(-\frac{2i}{\omega\hbar}V_{qp}\hat{x}\hat{y}\right)\exp\left(-\frac{i\tau}{2\hbar}\hat{T}_x\right),$$

where we noted

$$\int_0^{\frac{t_0}{2}} V_{qp}\sin(\omega t)\hat{x}\hat{y}dt = 2V_{qp}\frac{\hat{x}\hat{y}}{\omega}.$$

Introducing $\alpha = \dfrac{V_{qp}}{\omega\hbar\pi}$ in order to simplify notation and setting the lattice constant to unity, we can simplify the expression for $\hat{U}$ by noting

$$\exp(2i\pi\alpha\hat{x}\hat{y})\, c^{\dagger}_{x,y+1} c_{x,y} \exp(-2i\pi\alpha\hat{x}\hat{y}) = c^{\dagger}_{x,y+1} c_{x,y} \exp(2\pi i\alpha x)\,.$$

This identity can be used to evaluate the time evolution operator after m periods, which in the limit $\frac{\jmath t}{\hbar} \ll 1$ may be written as

$$\hat{U}(t = mt_0) = \exp\left(-\frac{it}{\hbar}\hat{H}_{\text{eff}}\right),$$

where

$$\hat{H}_{\text{eff}} \approx -J\sum_{x,y}\left[\hat{c}^{\dagger}_{x+1,y}\hat{c}_{x,y} + \hat{c}^{\dagger}_{x,y+1}\hat{c}_{x,y}e^{2\pi i\alpha x} + \text{h.c.}\right],$$

as presented by Sørensen *et al.* [21]. The physical interpretation of H_{eff} is that it describes the behavior of a charged particle on a lattice with a magnetic flux of $\alpha\Phi_0$, where Φ_0 is the phase aquired by the particle going through each unit cell, and hence the procedure introduces an effective artificial magnetic field in the lattice [21]. The form of the Peierls phase in the Hamiltonian is the one obtained from the Landau gauge.

2.1.2 Modification of Sørensen's proposal

The approach to obtain an artificial magnetic field for cold atoms in an optical lattice suggested by Sørensen *et al.* [21] discussed in Sec 2.1.1 was presented in the context of the Bose-Hubbard model, but ignores interactions and is not specific to bosons. The same procedure could equally well be applied to fermions. We consider a model of spinless fermions (corresponding to only one available hyperfine state for cold atoms) with Hamiltonian

$$\hat{H} = -\mathcal{J}\sum_{\langle i,j\rangle}(\hat{c}^{\dagger}_i\hat{c}_j + \hat{c}^{\dagger}_j\hat{c}_i), \tag{2.1}$$

where $\hat{c}^{\dagger}_i$ and $\hat{c}_i$ are fermionic creation and annihilation operators respectively at site i, $\hat{n}_i = \hat{c}^{\dagger}_i\hat{c}_i$ is the number operator, and the notation $\langle i,j\rangle$ restricts the sum in the hopping term to nearest neighbours only. There can be no Hubbard-like interaction for spinless fermions, and since nearest neighbour interactions in an optical lattice system are weak, we postpone our discussion of interactions to Chapter 4. We assume the fermions hop on a square lattice and set the lattice constant to unity.

Our modification to the proposal in Ref. [21] is that we allow hopping to be turned on in both the x and y directions simultaneously, but with different strengths, rather than exclusively in just the x or the y direction. When hopping is turned on in the x-direction at time $t = nt_0$, hopping is also turned on in the y-direction with an amplitude $0 \leq \beta \leq 1$ relative to the hopping in the x-direction. At time $t = \left(n + \frac{1}{2}\right) t_0$, hopping is turned on in the y direction, and hopping in the x-direction is turned on with amplitude β relative to the hopping in the x-direction as illustrated in Fig. 2.2.

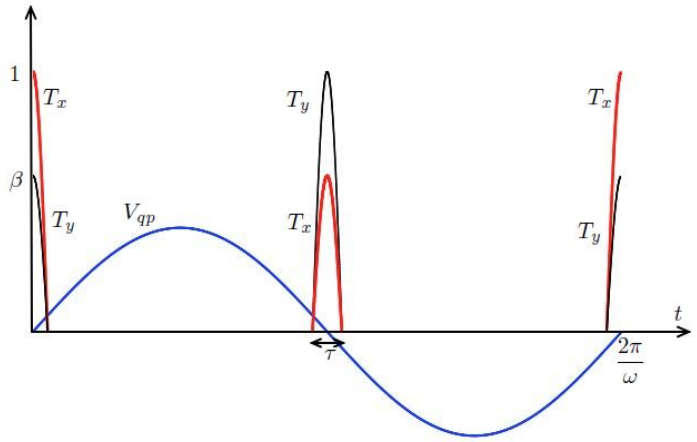

Figure 2.2: Time dependence of the hopping and the quadrupolar potential during the course of one period of the quadrupolar potential.

As before, the time evolution operator after m periods may be written as $\hat{U}(t = mt_0) = \hat{U}(t = t_0)^m$, and

$$\hat{U}\left(t = mt_0\right) = \left[e^{-\frac{i\tau}{2\hbar}\left(\beta\hat{T}_x + \hat{T}_y\right)} e^{2\pi i\alpha\hat{x}\hat{y}} e^{-\frac{i\tau}{\hbar}\left(\hat{T}_x + \beta\hat{T}_y\right)} e^{-2\pi i\alpha\hat{x}\hat{y}} e^{-\frac{i\tau}{2\hbar}\left(\beta\hat{T}_x + \hat{T}_y\right)}\right]^m, \tag{2.2}$$

where $\alpha = V_{qp}/\pi\hbar\omega$ as before. To lowest order in $\mathcal{J}\tau/\hbar$ we can write this in the form

$$\hat{U} = e^{-\frac{i\hat{H}_{\text{eff}}t}{\hbar}},$$

where the effective Hamiltonian is

$$\hat{H}_{\text{eff}} = -J_0 \sum_{x,y} \left\{ \left[\left(1 + \beta e^{2\pi i \alpha x}\right) \hat{c}^{\dagger}_{x,y+1} \hat{c}_{x,y} + \text{h.c.} \right] + \left[\left(\beta + e^{2\pi i \alpha y}\right) \hat{c}^{\dagger}_{x+1,y} \hat{c}_{x,y} + \text{h.c.} \right] \right\}, \quad (2.3)$$

with $J_0 = \tau \mathcal{J}/t_0$. [2]

The effective Hamiltonian implies that the artificial magnetic field is modified from Ref. [21]. A more conventional way to write the effective Hamiltonian is in the form

$$\hat{H}_{\text{eff}} = -\sum_{ij} \left[t_{ij} e^{\frac{ie}{\hbar} \int_j^i \vec{A} \cdot d\vec{l}} \hat{c}^{\dagger}_i \hat{c}_j + \text{h.c.} \right]. \quad (2.4)$$

This form makes clear that the Hamiltonian has spatially varying hopping and a spatially varying artificial vector potential. We can hence identify the amplitude of the hopping in the x and y directions:

$$|t_{x+1,y}| = J_0 \sqrt{1 + \beta^2 + 2\beta \cos(2\pi\alpha y)}, \quad (2.5)$$

$$|t_{x,y+1}| = J_0 \sqrt{1 + \beta^2 + 2\beta \cos(2\pi\alpha x)}, \quad (2.6)$$

and the components of the vector potential.

$$A_x = \frac{\hbar}{e} \tan^{-1} \left(\frac{\sin(2\pi\alpha y)}{\beta + \cos(2\pi\alpha y)} \right),$$

$$A_y = \frac{\hbar}{e} \tan^{-1} \left(\frac{\beta \sin(2\pi\alpha x)}{1 + \beta \cos(2\pi\alpha x)} \right).$$

Having the components of the vector potential, we may calculate that the magnetic field, $\vec{B} = \vec{\nabla} \times \vec{A}$, is directed along the z direction, with

$$B_z = (2\pi\alpha) \frac{\hbar}{e} \left(\frac{\beta^2 + \beta \cos(2\pi\alpha x)}{1 + \beta^2 + 2\beta \cos(2\pi\alpha x)} - \frac{1 + \beta \cos(2\pi\alpha y)}{1 + \beta^2 + 2\beta \cos(2\pi\alpha y)} \right). \quad (2.7)$$

It is worth noting that if in the above expression we set $\beta = 0$, then $B_z = -\dfrac{2\pi\hbar}{e}\alpha$, corresponding to a uniform flux of $\alpha\Phi_0$ through each unit cell and the hopping $t_{x+1,y} = t_{x,y+1} = J_0$ is spatially uniform, which is exactly the situation considered by Sørensen *et al.* Additionally, if $\beta = 1$, then there is no magnetic field, however, the hopping is still spatially periodic.

[2] There are additional terms that appear in the effective Hamiltonian of the order of $(\tau\mathcal{J})^2$ and higher, which are truncated here. A brief discussion of these is presented in Appendix A.

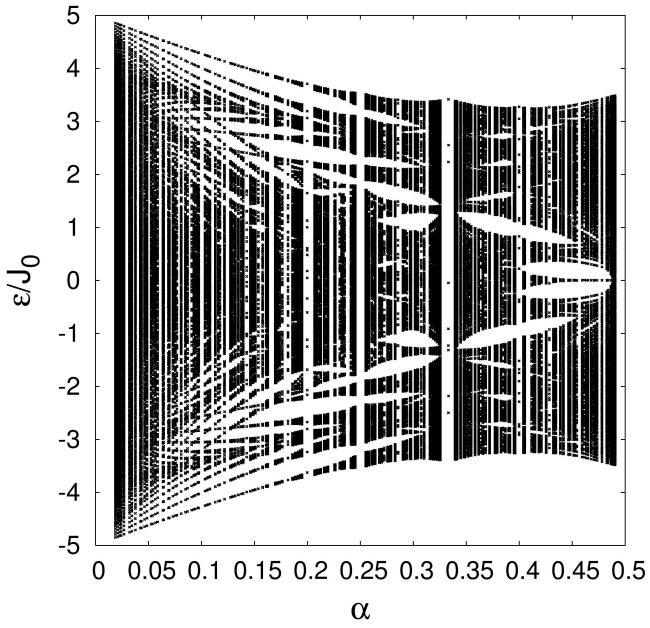

Figure 2.3: Spectrum as a function of α for a 197 by 197 lattice when $\beta = 0.25$. Due to the periodic hopping and non-zero artificial magnetic field, the spectrum has some similarities with the Hofstadter spectrum.

2.2 Hofstadter Spectrum

The magnetic field we derived in Eq. (2.7) has contributions from a spatially uniform piece with magnitude $\frac{2\pi\hbar\alpha}{e}$ and a piece that is spatially periodic in both the x and y directions. As noted above, if $\beta = 0$, the hopping amplitude is J_0 and the field is uniform with strength $\frac{2\pi\hbar\alpha}{e}$, corresponding to a flux of $\alpha\Phi_0$ per plaquette as found in Ref. [21] leading to a Hofstadter spectrum as illustrated in Fig. 2.1. If $\beta = 1$, then $B_z = 0$, but the hopping parameters are still spatially periodic. At β intermediate between 0 and 1, both the hopping and the magnetic field are spatially periodic in x and y. This illustrates the essential difference between the model we consider and previous work on quantum particles in a periodic magnetic field on a lattice in that there is spatial periodicity of $1/\alpha$ in the *amplitude* of the hopping as well as its phase. For finite β the spectrum as a function of α is reminiscent of the Hofstadter spectrum. This characteristic of our model is illustrated for $\beta = 0.25, 0.50$ and 1.00 in Figs. 2.3, 2.4 and 2.5. Interestingly, the strongest echo of the Hofstadter butter-

fly is seen when $\beta = 1$.

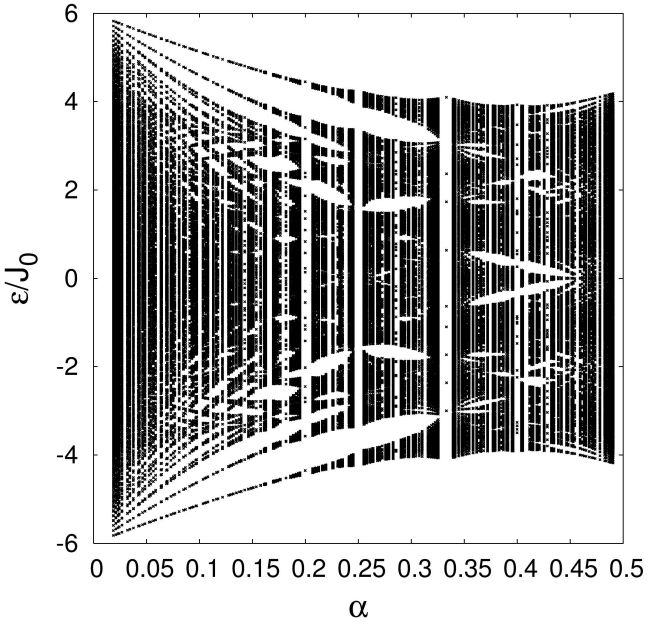

Figure 2.4: Energy spectrum as a function of α for a 197 by 197 lattice when $\beta = 0.5$.

Cold atoms in optical lattices also experience a trapping potential of the general form:

$$V_{\text{trap}} = \sum_i V(\vec{r}_i)\hat{c}_i^\dagger \hat{c}_i,$$

where $V(\vec{r}_i)$ is the magnitude of the trapping potential at site $\vec{r}_i$ [66]. This trapping potential breaks the translational symmetry of the lattice and might be expected to have some effects on the existence or observability of a Hofstadter spectrum. If we consider a harmonic trapping potential in two dimensions of the form $V(x,y) = v_0(x^2+y^2)$, where the parameter v_0 controls the strength of the trap and the positions on the lattice x and y are measured in units of the lattice constant, the parameter that controls the relative strength of the trap is v_0/J_0. Exact diagonalization calculations by P. Smith [66] suggest that for both the model considered here and the Hofstadter butterfly, signatures of the Hofstadter spectrum should be visible in the density of states versus position even for $v_0/J \simeq 0.001$, corresponding to a strong harmonic trap.

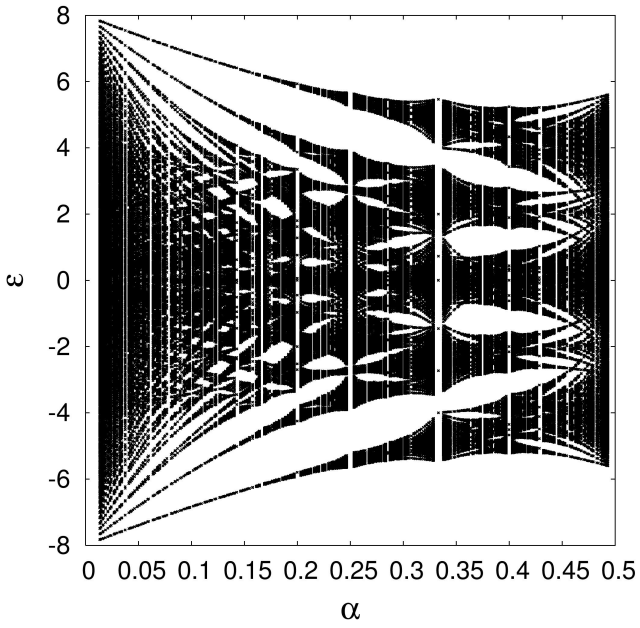

Figure 2.5: Spectrum as a function of α for a 197 by 197 lattice when $\beta = 1$: there is no artificial magnetic field, yet due to the periodic hopping, the spectrum has some similarities with the Hofstadter spectrum [57]. Copyright 2011 by the American Physical Society

2.3 Summary

In conclusion, in this chapter, we discussed a particular scheme for realizing an unusual tight-binding model in a cold atom system. We presented the resulting Hofstadter butterfly-like spectra associated with this model for several values of the parameter β. The lattice model given in Eq. (2.3) has a very interesting limit when there is an average of half a flux quantum per plaquette ($\alpha = 1/2$). We will discuss this limit of the model and the low energy birefringent fermionic excitations that arise in Chapter 3.

Chapter 3

Birefringent Dirac Fermions

There has been much recent interest in systems in which low energy excitations can be described using Dirac fermions [67, 68]. The main result in this chapter is that for the lattice model we introduced in Chapter 2, when there is an average of half a flux quantum per plaquette, at half filling, the low-energy degrees of freedom can be described by a Dirac Hamiltonian with the unusual property that the doubly degenerate Dirac cones for massless fermions splits into two cones with distinct slopes. This is analogous to a situation in which there are two speeds of light for fermionic excitations, similar to birefringence of light in crystals such as calcite (Fig. 3.1). This is a consequence of the fact that chiral symmetry is broken in the kinetic energy rather than via mass terms. We discuss the meaning of broken chiral symmetry in this model and explore the effects of various perturbations to the non-interacting theory, such as staggered potentials and topological defects. We postpone the discussion of interaction effects to Chapter 4.

3.1 Tight-binding Model

We start from the tight-binding Hamiltonian we introduced in Chapter 2, when there is an average of half a flux quantum per plaquette (i.e. $\alpha = 1/2$). The expression for the effective Hamiltonian then reads:

$$\hat{H}_{\text{eff}} = -J_0 \sum_{x,y} [(1+\beta e^{\pi i x}) c^{\dagger}_{x,y+1} c_{x,y} + \text{h.c.}] + [(\beta + e^{\pi i y}) c^{\dagger}_{x+1,y} c_{x,y} + \text{h.c.}], \qquad (3.1)$$

Figure 3.1: Birefringence of light and formation of split beams of light in calcite [69].

In the above Hamiltonian, if x is even, then the hopping in the y direction will be $J_0(1+\beta) = J_+$, and if x is odd, then the hopping along the y direction will be $J_0(1-\beta) = J_-$. If y is even, then the hopping along the x direction is $J_0(1+\beta) = J_+$, and for y odd, the hopping along the x direction is $-J_0(1-\beta) = -J_-$. These four values of the hopping are the only ones allowed, which allows us to reduce the problem to a tight-binding model with a 4 site unit cell illustrated in Fig. 3.2 in which the 4 sites of the plaquette are labelled as A, B, C, and D.

Rewriting the hopping Hamiltonian in terms of Fourier transformed fermionic operators

$$c_{iX} = \sum_k C_{k_X} e^{i\vec{k}\cdot\vec{r}_i},$$

where $X = A, B, C$ or D leads to

$$\hat{H} = \sum_k \Psi_k^* \begin{pmatrix} 0 & -2J_+\cos k_y & -2J_+\cos k_x & 0 \\ -2J_+\cos k_y & 0 & 0 & 2J_-\cos k_x \\ -2J_+\cos k_x & 0 & 0 & -2J_-\cos k_y \\ 0 & 2J_-\cos k_x & -2J_-\cos k_y & 0 \end{pmatrix} \Psi_k, \qquad (3.2)$$

with $\Psi_k^T = (C_{kA}, C_{kB}, C_{kC}, C_{kD})$ and the lattice constant set to unity.

The energy eigenvalues are

$$\varepsilon_{k,\pm,\pm} = \pm 2J_\pm \sqrt{\cos^2(k_x) + \cos^2(k_y)}, \qquad (3.3)$$

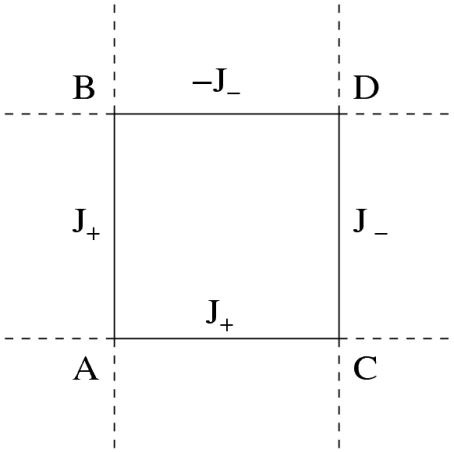

Figure 3.2: Unit cell of tight binding model with hopping parameters indicated [57]. Copyright 2011 by the American Physical Society.

as illustrated in Fig. 3.3.

We note that when $\beta = 1$, $J_- = 0$, so there will be a flat band at $\varepsilon = 0$ and a dispersing band associated with J_+. It is also worth noting that near the points $(k_x = \pm\pi/2, k_y = \pm\pi/2)$ in the Brillouin zone, e.g. when $k_x = \pi/2 - \delta k_x$ and $k_y = \pi/2 - \delta k_y$, the energy eigenvalues read:

$$\varepsilon_{k/\pm,\pm} = \pm 2J_\pm \sqrt{\delta k_x^2 + \delta k_y^2},$$

for small values of δk_x and δk_y, as illustrated in Fig. 3.4. This shows that in the vicinity of the four points $\vec{K} = (\pm\pi/2, \pm\pi/2)$ at the corners of the Brillouin zone, the energy spectrum has a Dirac form, and hence there will be Dirac cones with two different Fermi velocities corresponding to hopping energies $J_\pm$. When $\beta = 0$, the two slopes are identical, whereas as $\beta \to 1$, the J_- band becomes flat, and the J_+ band remains as a cone. When $\beta = 1$, the A, B, and C sites form a Lieb lattice, which is well-known to have a dispersion with a single Dirac cone and a flat band [70, 71, 72]. There have been recent suggestions on how to implement the Lieb lattice for cold atoms in optical lattices [70, 72]. When $\beta \neq 1$, the underlying Dirac structure of the problem is exposed, allowing us to understand this unusual dispersion from a symmetry point of view.

It is worth mentioning that in a hexagonal lattice such as graphene, whose low energy excitations can be described as four component Dirac fermions, there are two inequivalent

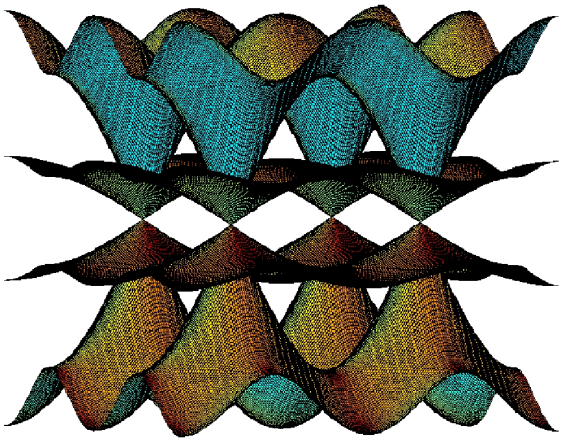

Figure 3.3: Energy dispersion showing the four bands of Eq. (3.3). Note the four Dirac points at the corner of the Brillouin zone.

Dirac points at the corners of the Brillouin zone whereas in the square lattice model we study,[1] the Dirac points at the four corners of the Brillouin zone are equivalent, meaning that they are related by a reciprocal lattice vector.

In the vicinity of the Dirac point $\vec{K} = \left(\frac{\pi}{2}, \frac{\pi}{2}\right)$, we may write the normalized eigenstates as

$$\tilde{\Psi}_1 = \frac{1}{\sqrt{2}} \begin{pmatrix} 1 \\ -\sin\theta \\ -\cos\theta \\ 0 \end{pmatrix}, \tilde{\Psi}_2 = \frac{1}{\sqrt{2}} \begin{pmatrix} 1 \\ \sin\theta \\ \cos\theta \\ 0 \end{pmatrix}, \tilde{\Psi}_3 = \frac{1}{\sqrt{2}} \begin{pmatrix} 0 \\ \cos\theta \\ -\sin\theta \\ 1 \end{pmatrix}, \tilde{\Psi}_4 = \frac{1}{\sqrt{2}} \begin{pmatrix} 0 \\ -\cos\theta \\ \sin\theta \\ 1 \end{pmatrix},$$

with $k_x = |\vec{k}|\cos\theta$ and $k_y = |\vec{k}|\sin\theta$ and where $\tilde{\Psi}_1$ and $\tilde{\Psi}_2$ correspond to eigenvalues ε_{++} and ε_{+-} respectively and $\tilde{\Psi}_3$ and $\tilde{\Psi}_4$ correspond to the eigenvalues ε_{+-} and ε_{--} respectively.

The linear combination $\tilde{\Psi}_1 + \tilde{\Psi}_2$ corresponding to fast (J_+) excitations, has non-zero amplitude only on the A sites, and the linear combination $\tilde{\Psi}_3 + \tilde{\Psi}_4$ has nonzero amplitude only on the D sites corresponding to slow (J_-) excitations. Any other state will break up into

[1] Ref. [73] demonstrates Dirac points in a square lattice model closely related to our model – the structure of the hopping is such that it is not left-right and up-down symmetric when the parameter $m \neq 0$ which leads to a gap in the spectrum, in contrast to our model in which hopping is left-right and up-down symmetric.

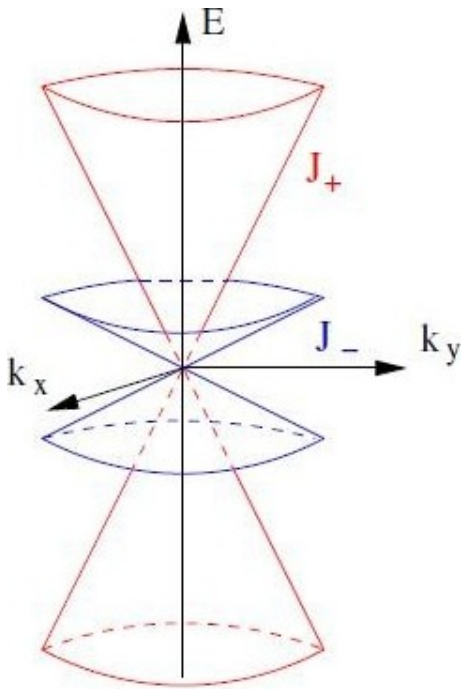

Figure 3.4: Energy dispersion illustrating the two Dirac cones with distinct Fermi velocities [57]. Copyright 2011 by the American Physical Society.

both fast and slow fermionic excitations, analogous to fast and slow modes in an optically birefringent medium.

3.2 Dirac-like Hamiltonian

Expanding the Hamiltonian around the Dirac point $\vec{K} = (\pi/2, \pi/2)$, we can write

$$H_k = 2 \begin{pmatrix} 0 & J_+\tilde{k}_y & J_+\tilde{k}_x & 0 \\ J_+\tilde{k}_y & 0 & 0 & -J_-\tilde{k}_x \\ J_+\tilde{k}_x & 0 & 0 & J_-\tilde{k}_y \\ 0 & -J_-\tilde{k}_x & J_-\tilde{k}_y & 0 \end{pmatrix}, \tag{3.4}$$

with $\vec{\tilde{k}} = \vec{K} - (\pi/2, \pi/2)$. H_k can be cast in terms of Pauli matrices as follows:

$$H_k = 2J_0 \left[\tilde{k}_x (\sigma_1 \otimes \sigma_3) + \tilde{k}_x \beta (\sigma_1 \otimes I_2) + \tilde{k}_y (I_2 \otimes \sigma_1) + \tilde{k}_y \beta (\sigma_3 \otimes \sigma_1) \right], \tag{3.5}$$

where we introduce a non-standard representation of the gamma matrices: $\gamma_0 = \sigma_3 \otimes \sigma_3$, $\gamma_1 = \sigma_2 \otimes I_2$, $\gamma_2 = \sigma_3 \otimes \sigma_2$, $\gamma_3 = -\sigma_1 \otimes I_2$ and $\gamma_5 = -\sigma_3 \otimes \sigma_1 = \gamma_0\gamma_1\gamma_2\gamma_3$. The matrices γ_0, γ_1, γ_2, and γ_3 respect the Clifford algebra $\gamma_\mu\gamma_\nu + \gamma_\nu\gamma_\mu = 2\delta_{\mu\nu}$.[2] This allows us to write the Hamiltonian as $\hat{H}_k = \hat{H}_0 + \beta\hat{H}_1$ where

$$\hat{H}_0 = 2J_0 \left[(i\gamma_0\gamma_1)\, \tilde{k}_x + (i\gamma_0\gamma_2)\, \tilde{k}_y \right],$$

and

$$\hat{H}_1 = 2J_0 \left[\gamma_3 \tilde{k}_x + \gamma_5 \tilde{k}_y \right].$$

In the limit $\beta = 0$, $\hat{H}$ has the form of a Dirac Hamiltonian with eigenvalues $E_k = \pm 2J_0|\tilde{k}|$. When $\beta \neq 0$, the eigenvalues of $\hat{H}$ are $E_k = \pm 2J_\pm|\tilde{k}|$.

3.3 Chiral Symmetry

The dimension of the minimal representation of a Clifford algebra in 2+1 dimensions is 2, allowing for the 2×2 Pauli matrices as a choice for the γ matrices. For a two dimensional time reversal symmetric system on the lattice, where the square of the time reversal operator is equal to the identity, it has been shown that it is algebraically necessary to have a minimal dimension of 4 [74]. Hence, we have a non-minimal 4×4 representation which leads to a freedom in the choice of the γ_0 matrix, i.e. a matrix with $(\gamma_0)^2 = I_4$ that anticommutes with γ_1 and γ_2. Candidates for γ_0 are $\{\gamma_0, \gamma_0\gamma_3, \gamma_0\gamma_5, \gamma_1\gamma_2\}$. The matrices $\{\gamma_0, \gamma_0\gamma_3, \gamma_0\gamma_5\}$ form a triplet and $\gamma_1\gamma_2$ forms a singlet with respect to the SU(2) "chiral"-symmetry group with generators $\{\frac{1}{2}\gamma_3, \frac{1}{2}\gamma_5, \frac{1}{2}\gamma_{35}\}$ (where $\gamma_{35} \equiv \gamma_3\gamma_5$). Each different choice of γ_0 corresponds to a different labelling of the four sites in the unit cell. The elements of the chiral group generate transformations between each labelling. For example, the generator γ_5 translates

[2] This notation differs from the notation used in Ref. [57]. Namely, we have used a Euclidean metric $\delta_{\mu\nu}$ rather than Minkowski metric $g_{\mu\nu}$.

the plaquette indices to the labelling of the neighbouring lattice cell along the y-direction, whilst γ_3 translates the plaquette indices to the neighbouring cell in the x-direction:

$$e^{i\frac{\pi}{2}\gamma_5}\begin{pmatrix} c_A \\ c_B \\ c_C \\ c_D \end{pmatrix} = i\begin{pmatrix} c_B \\ c_A \\ -c_D \\ -c_C \end{pmatrix}, \qquad e^{i\frac{\pi}{2}\gamma_3}\begin{pmatrix} c_A \\ c_B \\ c_C \\ c_D \end{pmatrix} = i\begin{pmatrix} c_C \\ c_D \\ c_A \\ c_B \end{pmatrix}. \tag{3.6}$$

Similarly, γ_{35} translates the plaquette one lattice cell along the x- and one lattice cell along

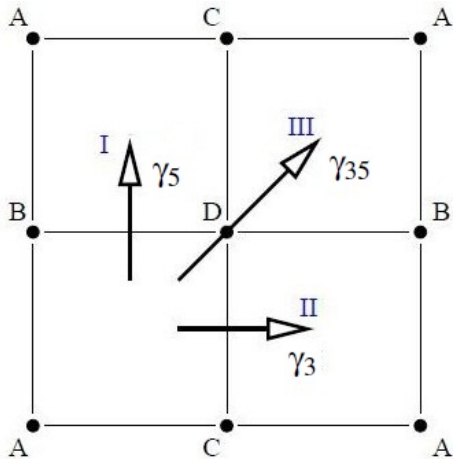

Figure 3.5: Illustration of relabelling symmetries generated by γ_3, γ_5 and γ_{35}.

the y- direction.

$$e^{i\gamma_{35}\pi/2}\begin{pmatrix} c_A \\ c_B \\ c_C \\ c_D \end{pmatrix} = i\begin{pmatrix} -c_D \\ -c_C \\ c_B \\ c_A \end{pmatrix}.$$

The symmetries due to the above rotations are illustrated in Fig. 3.5.

When $\beta = 0$, the elements of the chiral group are symmetries of H_k. When $\beta \neq 0$, the presence of the γ_3 and γ_5 terms in H_k breaks the chiral symmetry and shifts along either the x- or y-directions do not leave H_k invariant. This manifest chiral symmetry breaking is inherently different from the conventional notion of spontaneous chiral symmetry breaking in field theoretical models which is the signature of mass generation.

An additional discrete symmetry of the Hamiltonian (which arises from the hopping structure in H_k) that holds even when $\beta \neq 0$ is

$$\Gamma = \frac{i}{2}(\gamma_2\gamma_3 + \gamma_1\gamma_5) - \frac{i}{2}(\gamma_1\gamma_3 + \gamma_2\gamma_5),$$

which corresponds to a reflection about the diagonal AD in the unit cell, with $c_A \to c_A$, $c_B \to c_C$, $c_C \to c_B$ and $c_D \to -c_D$. The action of Γ on H_k is to exchange k_x and k_y.

3.4 Staggered potential

Staggered on-site potentials are a natural perturbation to H_k in the context of cold atoms on an optical lattice. The most general form of a staggered potential that we can write down takes the form

$$\begin{pmatrix} \Delta_A & 0 & 0 & 0 \\ 0 & \Delta_B & 0 & 0 \\ 0 & 0 & \Delta_C & 0 \\ 0 & 0 & 0 & \Delta_D \end{pmatrix},$$

where Δ_x is the staggered potential on site x. It is convenient to rewrite the contribution to the Hamiltonian in terms of γ matrices as

$$\hat{H}_\Delta = \sum_k \psi_k^\dagger \left[\Delta_0 I_4 + \Delta_1\gamma_0 + \Delta_2(i\gamma_1\gamma_3 + i\gamma_2\gamma_5) + \Delta_3(i\gamma_1\gamma_3 - i\gamma_2\gamma_5)\right]\psi_k, \tag{3.7}$$

where we made use of the basis $\{I, \gamma_0, i\gamma_1\gamma_3, i\gamma_2\gamma_5\}$ for 4 by 4 diagonal matrices, recalling that

$$\gamma_0 = \begin{pmatrix} 1 & 0 & 0 & 0 \\ 0 & -1 & 0 & 0 \\ 0 & 0 & -1 & 0 \\ 0 & 0 & 0 & 1 \end{pmatrix}, \quad -i\gamma_2\gamma_5 = \begin{pmatrix} 1 & 0 & 0 & 0 \\ 0 & -1 & 0 & 0 \\ 0 & 0 & 1 & 0 \\ 0 & 0 & 0 & -1 \end{pmatrix}, \quad -i\gamma_1\gamma_3 = \begin{pmatrix} 1 & 0 & 0 & 0 \\ 0 & 1 & 0 & 0 \\ 0 & 0 & -1 & 0 \\ 0 & 0 & 0 & -1 \end{pmatrix}.$$

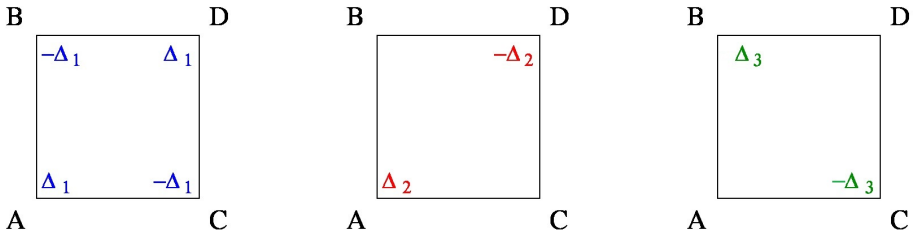

Figure 3.6: The three staggered potentials Δ_1, Δ_2 and Δ_3 on the four sites of a square lattice.

We may set $\Delta_0 = 0$ since this can be compensated with a uniform shift of the chemical potential. The remaining three non-trivial terms, Δ_1, Δ_2 and Δ_3 are illustrated in Fig. 3.6. The Δ_1 term violates chiral symmetry in the usual way, meaning that it introduces a "mass" term in the energy spectrum, but is Lorentz invariant and introduces a gap in the dispersion of the fermions

$$E_k = \pm\sqrt{\Delta_1^2 + 4J_\pm^2 k^2}. \tag{3.8}$$

A comparision of the spectrum when $\Delta_1 = 0$ and when $\Delta_1 \neq 0$ is shown in Fig. 3.7.

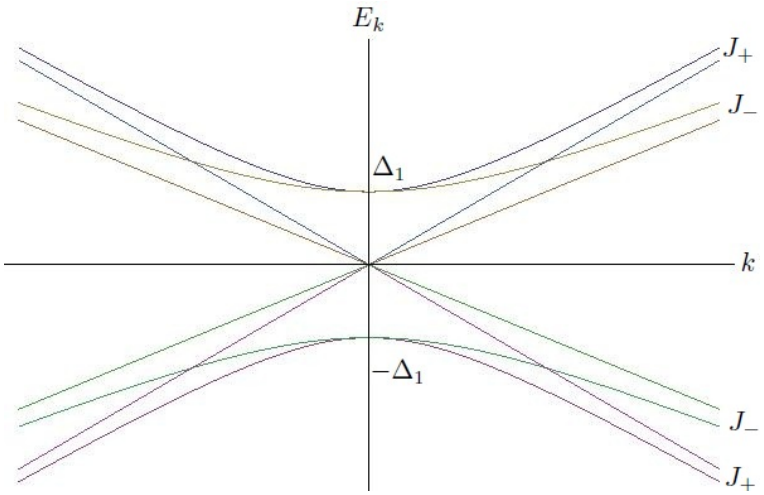

Figure 3.7: Energy spectrum as a function of k when $\Delta_1 \neq 0$ and $\Delta_1 = 0$.

When $\beta = 1$ there are flat bands at $E = \pm\Delta_1$ that intersect the J_+ bands only at $(k_x, k_y) = (0,0)$. The birefringence property discussed above is unaffected by the Δ_1 term. We combine $i\gamma_1\gamma_3$ and $i\gamma_2\gamma_5$ into a Lorentz invariant term (Δ_2) and a Lorentz violating term (Δ_3).

There are two cases in which we have obtained simple analytic solutions for the spectrum: Case I): $\Delta_1 \neq 0$, $\Delta_2 \neq 0$, $\Delta_3 = 0$, for which

$$E_k = \begin{cases} \Delta_2 \pm \sqrt{(\Delta_1+\Delta_2)^2 + 4J_+^2 k^2} \\ -\Delta_2 \pm \sqrt{(\Delta_1-\Delta_2)^2 + 4J_-^2 k^2} \end{cases},$$

Case II): $\Delta_1 \neq 0$, $\Delta_2 = 0$, $\Delta_3 \neq 0$, for which

$$E_k = \begin{cases} \Delta_3 \pm \sqrt{(\Delta_1-\Delta_3)^2 + 4J_+^2 k_y^2 + 4J_-^2 k_x^2} \\ -\Delta_3 \pm \sqrt{(\Delta_1+\Delta_3)^2 + 4J_+^2 k_x^2 + 4J_-^2 k_y^2} \end{cases}.$$

In case I) the dispersion is isotropic in momentum space and there are flat bands when $\beta = 1$, whereas in case II), the dispersion is anisotropic in momentum space, with the anisotropy governed by β through $J_\pm$. In both cases, there is a shift in the spectrum and at least one set of massive modes (however in both cases there can be a set of massless modes whose dispersion is given by the upper half of a cone if $\Delta_1 = \pm\Delta_{2,3}$ and $\Delta_0 = \mp\Delta_{2,3}$).

3.4.1 Staggered Hopping

In addition to staggered potentials, another case where one can obtain analytic expressions for the dispersion is if there are mass terms of the form $i\gamma_0\gamma_3$ and $i\gamma_0\gamma_5$. Physically these correspond to staggered hopping. Roy *et al.* [76] have shown that a Hamiltonian of the following form:

$$H_k = i\gamma_0\gamma_1 k_x + i\gamma_0\gamma_2 k_y - \beta\gamma_3 k_x - \beta\gamma_5 k_y - mi\gamma_0\gamma_3,$$

has the energy spectrum:

$$\varepsilon_k = \pm\sqrt{(1+\beta^2)|k|^2 + m^2 \pm 2\beta|k|^2\sqrt{1+\frac{m^2k_y^2}{|k|^4}}},$$

which does not preserve the property of birefringence. However, it is worth noting that for the case where $k = 0$, there is a gap of $2m$ in the spectrum and that the minimum energy can occur at a non-zero value of k [76]. One can show that an analogous calculation with mass term $i\gamma_0\gamma_5$ yields a result similar to that for the term $i\gamma_0\gamma_3$ but with mk_y replaced by mk_x.

3.5 Topological Defects

Zero energy modes can arise when there are topologically non-trivial mass terms in systems that are described by the Dirac Hamiltonian [76]. As we saw in Sec.3.4, the term $\Delta_1\gamma_0$ generates a gap in the energy spectrum in the Dirac-like Hamiltonian under study.
The simplest topological defect we may construct is of the domain wall type, by choosing $\Delta_1(x)$ to be a function of position, so that $\Delta_1(0) = 0$ and $\lim_{x\to\infty}\Delta_1(x) = \Delta_1$ and $\lim_{x\to-\infty}\Delta_1(x) = -\Delta_1$, where Δ_1 is a constant with smooth interpolation between these limits. The real space Dirac equation becomes

$$\begin{pmatrix} -E-\Delta_1 & 2J_+i\partial_y & 2J_+i\partial_x & 0 \\ 2J_+i\partial_y & -E+\Delta_1 & 0 & -2J_-i\partial_x \\ 2J_+i\partial_x & 0 & -E+\Delta_1 & 2J_-i\partial_y \\ 0 & -2J_-i\partial_x & 2J_-i\partial_y & -E-\Delta_1 \end{pmatrix} \begin{pmatrix} \psi_A \\ \psi_B \\ \psi_C \\ \psi_D \end{pmatrix} = 0. \tag{3.9}$$

If $\beta = 0$, the solutions are well known [75]. When $\beta \neq 0$, we can find zero energy bound states with different spatial extents for the $\pm$ solutions:

$$\psi_+(x) = e^{-\kappa_+\int_0^x ds\Delta_1(s)}u_+; \quad \psi_-(x) = e^{-\kappa_-\int_0^x ds\Delta_1(s)}u_-,$$

where $u_+ = (1,0,i,0)$, $u_- = (0,-i,0,1)$, and $\kappa_\pm = 1/2J_\pm$. The $\kappa_\pm$ are the the inverse of the characteristic length scales for the zero modes in the presence of the domain wall.

In addition to the domain wall defects studied here, another class of defects, namely vortices, was studied by Roy *et al.* [76]. They constructed simultaneous vortices in the kinetic energy (via β) and in the mass terms $i\gamma_0\gamma_3$ and $i\gamma_0\gamma_5$ (corresponding to staggered hoppings in Sec.3.4.1). They found that the ratio of the length scales associated with states centered on vortex and antivortex topological defects can vary arbitrarily with β without affecting the fractionalization of quantum numbers such as charge [76]. This mirrors the two different lengthscales for zero modes found here for domain wall defects. Roy [77] has also demonstrated that two lengthscale behaviour may be found for zero modes of special topological defects in graphene when there is both a real and a pseudo magnetic field present.

3.6 Summary

In this chapter, we started from the tight-binding Hamiltonian derived in Chapter 2 for the case where an average of half a flux quantum per plaquette. We showed that the low energy excitations of this Hamiltonian are birefringent fermions, with two distinct Fermi velocities, that remain massless despite breaking chiral symmetry. This is because chiral symmetry is broken in the kinetic energy rather than with a mass term. We studied the effect of staggered potentials on the birefringence property and found that Lorentz invariant staggered potentials preserved the birefringence property. We finally discussed the unusual zero modes that can result for birefringent fermions in the presence of a topological defect.

Chapter 4

Interacting Birefringent Fermions

The model we considered in Chapter 3 has no interactions between fermions. Interactions between fermions can lead to a range of possible phases. In this chapter, we study the model introduced in Chapter 3 when there are repulsive interactions between fermions (we consider lattice interactions but we do not worry about physical implementations of these interactions). Including nearest neighbour and next nearest neighbour terms, we search for possible ordered phases. We focus on low energy physics and treat interactions at a mean field level for a half-filled system. There has been some previous work on the effect of interactions in models similar to this one, such as the Lieb lattice (the $\beta = 1$ limit of the model studied here) in two dimensions at one-third, [78], but the work in this thesis is the first to consider $\beta \neq 0$ and 1. In Ref. [79], it was also shown that when spin-orbit coupling is taken into account, topologically nontrivial insulating phases may arise on the Lieb lattice.

4.1 Nearest-neighbour Interactions

The simplest interaction term for spinless fermions (e.g. a single occupied hyperfine level) is that of nearest neighbour interactions as the Pauli principle forbids the presence of an on-site Hubbard term in the Hamiltonian. We introduce such a term, assuming that all interactions have the same magnitude, V_0:

$$H_{\text{int}} = V_0 \sum_{\langle i,j \rangle} \hat{n}_i \hat{n}_j, \tag{4.1}$$

where $\langle i, j \rangle$ labels a sum over nearest neighbours. In the context of cold atoms, one might expect V_0 to be weak and we will address the stability of the birefringent semi-metal to these interactions. We have seen that birefringent fermions arise as low-energy excitations of the tight binding model introduced in Chapter 3, and since we are interested in the effects of interactions on birefringent fermions, we will also focus on the low energy limit of H_{int}.

Replacing fermionic annihilation operators, c_I, with fields ψ_I, we may write the full Lagrangian as $L = L_0 + L_\beta + L_{\text{int}}$, where the non-interacting terms $L_0 + L_\beta$ are (having set $2J_0$ to unity)

$$L_0 + L_\beta = \left\{ \sum_{\vec{r}} \bar{\psi}(\vec{r})\gamma_\mu \partial_\mu \psi(\vec{r}) + i\beta\bar{\psi}(\vec{r})\gamma_0\gamma_3\partial_x\psi(\vec{r}) + i\beta\bar{\psi}(\vec{r})\gamma_0\gamma_5\partial_y\psi(\vec{r}) \right\}, \tag{4.2}$$

and L_{int} is obtained from H_{int}. We can represent the generating functional as an imaginary time path integral over Grassmann-valued fields ψ and $\bar{\psi}$.

$$\mathcal{Z} = \int [\mathcal{D}\bar{\psi}][\mathcal{D}\psi] e^{-S}, \tag{4.3}$$

where the action $S = \int_0^\beta d\tau \; L$, with τ the imaginary time.

The term L_{int} contains quartic terms. The approach we shall take to decouple these quartic terms is to introduce Hubbard Stratonovich fields so that the action becomes quadratic in the ψ fields. The Hubbard Stratonovich fields we consider correspond to order parameters that can be obtained through either a Hartree or a Fock decomposition of the interaction term. Before introducing Hubbard Stratonovich fields, recall that the Lagrangian for the interaction term can be written in terms of the number operators as follows:

$$L_{\text{int}} = -2V_0 \sum_{\vec{r}} \left[n_A n_B + n_A n_C + n_B n_D + n_C n_D \right], \tag{4.4}$$

when we consider only slow spatial variation in n_A, n_B, n_C, and n_D, which is equivalent to ignoring scattering between Dirac cones. It is useful to note that

$$\begin{aligned} n_A n_B + n_A n_C + n_B n_D + n_C n_D &= \frac{1}{4}\left[(n_A + n_B + n_C + n_D)^2 - (n_A - n_B - n_C + n_D)^2 \right] \\ &= \frac{1}{4}\left[(\bar{\psi}\gamma_0\psi)^2 - (\bar{\psi}\psi)^2 \right]. \end{aligned} \tag{4.5}$$

The expectation values $\langle\bar{\psi}\psi\rangle$ and $\langle\bar{\psi}\gamma_0\psi\rangle$ correspond to order parameters that arise in the Hartree channel. The first is staggered charge density wave order of the sort Δ_1 illustrated in Fig. 3.6 and the second renormalizes the chemical potential. We note that

$$\langle\bar{\psi}\psi\rangle = [\langle n_A\rangle - \langle n_B\rangle - \langle n_C\rangle + \langle n_D\rangle],$$

and

$$\langle\bar{\psi}\gamma_0\psi\rangle = [\langle n_A\rangle + \langle n_B\rangle + \langle n_C\rangle + \langle n_D\rangle].$$

The Fock terms are a little more complicated but may be obtained from $L_{\rm int}$ in Eq. (4.4) and may be summarized as:

$$L_{\rm Fock} = 2V_0 \sum_{\vec{r}} \bar{\psi}\left[\zeta_{01}\gamma_0\gamma_1 + \zeta_1 i\gamma_1 + \zeta_{03}\gamma_0\gamma_3 + \zeta_3 i\gamma_3 + \zeta_{02}\gamma_0\gamma_2 + \zeta_2 i\gamma_2 + \zeta_{05}\gamma_0\gamma_5 + \zeta_5 i\gamma_5\right]\psi, \tag{4.6}$$

where the ζ's can also be related to expectation values of the ψ's. We also note that:

$$(\bar{\psi}\gamma_0\gamma_1\psi)^2 + (\bar{\psi}i\gamma_1\psi)^2 + (\bar{\psi}\gamma_0\gamma_3\psi)^2 + (\bar{\psi}i\gamma_3\psi)^2 = -8\left[n_A n_C + n_B n_D\right],$$

and

$$(\bar{\psi}\gamma_0\gamma_2\psi)^2 + (\bar{\psi}i\gamma_2\psi)^2 + (\bar{\psi}\gamma_0\gamma_5\psi)^2 + (\bar{\psi}i\gamma_5\psi)^2 = -8\left[n_A n_B + n_C n_D\right].$$

Introducing Hubbard-Stratonovich fields χ, ϕ, and $\{\zeta_i\}$, where the mean field values $\chi \propto \langle\bar{\psi}\psi\rangle$, $\phi \propto \langle\bar{\psi}\gamma_0\psi\rangle$ and ζ_i encompasses the 8 ζs introduced above, we get

$$\mathcal{Z} = \int [\mathcal{D}\chi][\mathcal{D}\phi]\prod_i [\mathcal{D}\zeta_i] e^{-S[\chi]-S[\phi]-\sum_i S[\zeta_i]} \int [\mathcal{D}\bar{\psi}][\mathcal{D}\psi] e^{-S_0[\bar{\psi},\psi]-S_{mix}}, \tag{4.7}$$

where

$$S[\chi] = \frac{2}{V_0}\int_0^\beta d\tau \int d^2\vec{x}\ \ [\chi(\vec{x},\tau)]^2,$$

$$S[\phi] = \frac{2}{V_0}\int_0^\beta d\tau \int d^2\vec{x}\ \ [\phi(\vec{x},\tau)]^2,$$

$$S[\zeta_i] = \frac{2}{V_0}\int_0^\beta d\tau \int d^2\vec{x}\ \ [\zeta_i(\vec{x},\tau)]^2,$$

$$S_0[\bar{\psi},\psi] = \int_0^\beta d\tau\ \ (L_0 + L_\beta),$$

and

$$\begin{aligned} S_{mix} &= \int_0^\beta d\tau \int d^2\vec{x}\,[\chi\bar{\psi}\psi + i\phi\bar{\psi}\gamma_0\psi + \zeta_{01}\bar{\psi}\gamma_0\gamma_1\psi + \zeta_1\bar{\psi}(i\gamma_1)\psi + \zeta_{03}\bar{\psi}\gamma_0\gamma_3\psi \\ &\quad + \zeta_3\bar{\psi}(i\gamma_3)\psi + \zeta_{02}\bar{\psi}\gamma_0\gamma_2\psi + \zeta_2\bar{\psi}(i\gamma_2)\psi + \zeta_{05}\bar{\psi}\gamma_0\gamma_5\psi + \zeta_5\bar{\psi}(i\gamma_5)\psi]\,. \end{aligned}$$

A point to note in the action is that the coefficients of $S[\chi]$, $S[\phi]$ and $S[\zeta_i]$ differ by a factor of 2 from the value they would take if the Hubbard-Stratonovich fields corresponding only to Hartree terms or only to Fock terms were introduced into the action. The reason for this factor of 2 is that we treated Hartree and Fock terms with equal weight. Ultimately, if there is only one non-zero order parameter, then the critical value of the coupling, $\frac{1}{V_c}$, should be multiplied by 2.

We can integrate out the fermion fields to obtain the effective action for the Hubbard-Statonovich fields:

$$\int [\mathcal{D}\bar{\psi}][\mathcal{D}\psi] e^{-\int_0^\beta d\tau d^2\vec{x}\ \bar{\psi}M\psi} = \det M = e^{\ln(\det M)} = e^{\mathrm{Tr}(\ln \mathrm{M})}.$$

We may then write the generating functional as:

$$\begin{aligned} \mathcal{Z} &= \int [\mathcal{D}\bar{\psi}][\mathcal{D}\psi] \int [\mathcal{D}\chi][\mathcal{D}\phi] \prod_i [\mathcal{D}\zeta_i] e^{-S[\chi]-S[\phi]-\sum_i S[\zeta_i] - S_0[\bar{\psi},\psi] - S_{mix}} \\ &= \int [\mathcal{D}\chi][\mathcal{D}\phi] \prod_i [\mathcal{D}\zeta_i] e^{-S[\chi]-S[\phi]-\sum_i S[\zeta_i] + \mathrm{Tr}(\ln \mathrm{M})}, \end{aligned}$$

where the matrix M

$$\begin{aligned} M &= \gamma_\mu\partial_\mu + i\beta(\gamma_0\gamma_3\partial_x + \gamma_0\gamma_5\partial_y) + \chi + i\phi\gamma_0 + \zeta_{01}\gamma_0\gamma_1 + \zeta_1 i\gamma_1 + \zeta_{03}\gamma_0\gamma_3 + \zeta_3 i\gamma_3 + \zeta_{02}\gamma_0\gamma_2 \\ &\quad + \zeta_2 i\gamma_2 + \zeta_{05}\gamma_0\gamma_5 + \zeta_5 i\gamma_5 \\ &= G_\beta^{-1} + \chi + i\phi + \zeta_{01}\gamma_0\gamma_1 + \zeta_1 i\gamma_1 + \zeta_{03}\gamma_0\gamma_3 + \zeta_3 i\gamma_3 + \zeta_{02}\gamma_0\gamma_2 + \zeta_2 i\gamma_2 + \zeta_{05}\gamma_0\gamma_5 + \zeta_5 i\gamma_5, \end{aligned} \tag{4.8}$$

where

$$G_\beta^{-1} = \gamma_\mu\partial_\mu + i\beta(\gamma_0\gamma_3\partial_x + \gamma_0\gamma_5\partial_y),$$

is the inverse of the free propagator. M is thus the inverse of the full propagator in the presence of different types of ordering.

4.1.1 Saddle Point Equations

The simplest level of analysis to determine whether there is ordering or not for the various order parameters listed in Eq. (4.8) is to find equations that can be solved to determine the mean field phase transitions to these orders using the *Saddle Point Approximation*.
For each Hubbard-Stratonovich field F, the saddle point equation is given by $\frac{\delta S}{\delta F} = 0$. We can summarize these equations as follows:

$$\frac{4\chi}{V_0} = \mathrm{Tr}(M^{-1}), \tag{4.9}$$

$$\frac{4\phi}{V_0} = \mathrm{Tr}(i\gamma_0 M^{-1}), \tag{4.10}$$

$$\frac{4\zeta_i}{V_0} = \mathrm{Tr}(\Gamma_i M^{-1}), \tag{4.11}$$

where

$$\Gamma_i \in \{\gamma_0\gamma_1, i\gamma_1, \gamma_0\gamma_3, i\gamma_3, \gamma_0\gamma_2, i\gamma_2, \gamma_0\gamma_5, i\gamma_5\}.$$

In order to calculate M^{-1}, we express M in momentum space

$$\begin{aligned} M = {} & i\gamma_\mu k_\mu + i\beta(\gamma_0\gamma_3 ik_1 + \gamma_0\gamma_5 ik_2) + \chi + i\phi\gamma_0 + \zeta_{01}\gamma_0\gamma_1 + \zeta_1 i\gamma_1 + \zeta_{03}\gamma_0\gamma_3 \\ & + \zeta_3 i\gamma_3 + \zeta_{02}\gamma_0\gamma_2 + \zeta_2 i\gamma_2 + \zeta_{05}\gamma_0\gamma_5 + \zeta_5 i\gamma_5, \end{aligned}$$

and note that $MM^{-1} = I$. Hence, we need to solve:

$$\begin{aligned} & [\chi I + i(k_0+\phi)\gamma_0 + i(k_1+\zeta_1)\gamma_1 + i(k_2+\zeta_2)\gamma_2 + \gamma_0\gamma_3(\zeta_{03} - \beta k_1) + \gamma_0\gamma_5(\zeta_{05} - \beta k_2) \\ & + \zeta_{01}\gamma_0\gamma_1 + \zeta_{02}\gamma_0\gamma_2 + \zeta_3 i\gamma_3 + \zeta_5 i\gamma_5] M^{-1} = I. \end{aligned}$$

Solving the system of 10 saddle point equations simultaneously is a rather intimidating task, and not the simplest approach to understand the effects of interactions. The strategy

we shall take is to find the transitions for each order parameter individually, by searching for a solution in which all other Hubbard-Stratonovich fields are set to zero.
Now, for the case where only the χ or ϕ order parameters are non-zero, we must solve:

$$\{\chi I + i(k_0+\phi)\gamma_0 + i\gamma_1 k_1 + i\gamma_2 k_2 - \beta\gamma_0\gamma_3 k_1 - \beta\gamma_0\gamma_5 k_2\} M^{-1} = I.$$

Hence, the saddle point equation for χ is:

$$\frac{4\chi}{V} = 4\int \frac{d^3\vec{k}}{(2\pi)^3} \frac{\chi[\chi^2 + (k_0+\phi)^2 + (1+\beta^2)|\vec{k}|^2]}{[\chi^2 + (k_0+\phi)^2 + (1-\beta)^2|\vec{k}|^2][\chi^2 + (k_0+\phi)^2 + (1+\beta)^2|\vec{k}|^2]}.$$

If we set $\phi = 0$ and send $\chi \to 0$, then the critical interaction strength for χ ordering is:

$$\frac{1}{V_c} = \frac{1}{2}\int \frac{dk_x}{2\pi}\frac{dk_y}{2\pi}\int \frac{dk_0}{2\pi}\left\{\frac{1}{\chi^2 + k_0^2 + (1-\beta)^2|\vec{k}|^2} + \frac{1}{\chi^2 + k_0^2 + (1+\beta)^2|\vec{k}|^2}\right\}.$$

We determine the critical interaction strength for ordering in the Hartree channel χ from:

$$\frac{1}{V_c} = \frac{1}{8\pi^2}\int_{-1}^{1} dx \int_0^{\Lambda} dk \left\{\frac{k^2}{\chi^2 + k^2[(1-\beta)^2 + x^2\beta(2-\beta)]} + \frac{k^2}{\chi^2 + k^2[(1+\beta)^2 - x^2\beta(2+\beta)]}\right\},$$

by keeping terms that persist as $\chi \to 0$ and scale with the cutoff Λ, where $k_0 = kx$ and $|\vec{k}|^2 = k^2(1-x^2)$. Hence,

$$\frac{1}{V_c} = \frac{\Lambda}{4\pi^2}\left\{\frac{1}{(1-\beta)\sqrt{\beta(2-\beta)}}\tan^{-1}\left(\frac{\sqrt{\beta(2-\beta)}}{1-\beta}\right) + \frac{1}{2(1+\beta)\sqrt{\beta(2+\beta)}}\ln\left|\frac{1+\dfrac{1+\beta}{\sqrt{\beta(2+\beta)}}}{1-\dfrac{1+\beta}{\sqrt{\beta(2+\beta)}}}\right|\right\}.$$

In the limit $\beta \to 0$, this reduces to $\dfrac{1}{V_c} = \dfrac{\Lambda}{2\pi^2}$, which, if Fock terms are not included in the decomposition of H_{int} is renormalized as noted previously to $\dfrac{1}{V_c} = \dfrac{\Lambda}{\pi^2}$, in complete agreement with previous results [80]. The other auxiliary field, ϕ, which is physically equivalent to a shift in the chemical potential, gives us the following integral:

$$\frac{\phi}{V_0} = \frac{1}{2}\int \frac{dk_x}{2\pi}\frac{dk_y}{2\pi}\int \frac{dk_0}{2\pi}(k_0+\phi)\left\{\frac{1}{(k_0+\phi)^2 + (1-\beta)^2|\vec{k}|^2} + \frac{1}{(k_0+\phi)^2 + (1+\beta)^2|\vec{k}|^2}\right\}.$$

If $\phi = 0$, the integrand on the right-hand-side is odd in k_0, and hence the integral vanishes, Hence, $\phi = 0$ is a consistent solution of the equation for all V_0.

There are eight possible order parameters, ζ_i, in the Fock channel. Similarly to the Hartree channel, we will take the approach of solving for the critical interaction for each of these order parameters separately.

The equation we need to solve for the critical coupling associated with ζ_{01} is then:

$$\frac{\zeta_{01}}{V_{01}} = \int \frac{dk_x}{2\pi}\frac{dk_y}{2\pi}\int \frac{dk_0}{2\pi}\frac{\zeta_{01}(-k_0^2-(1-\beta^2)|k|^2+\zeta_{01}^2+2(k_x^2+k_0^2))}{(-k_0^2-(1-\beta^2)|k|^2+\zeta_{01}^2)^2+4(\beta^2k_0^2|k|^2+\zeta_{01}^2(k_0^2+k_x^2))}.$$

Therefore:

$$\begin{aligned}\frac{1}{V_{01}} &= \frac{1}{(2\pi)^3}\int_{-1}^{1}dx\int_0^{\Lambda}dk\ k^2\left[2k^2(1-x^2)\int_0^{2\pi}d\phi\frac{\cos^2\phi}{a^2+b^2\cos^2\phi}\right.\\ &\left.+(2k^2x^2+[\zeta_{01}^2-k^2x^2-(1-\beta^2)k^2(1-x^2)])\int_0^{2\pi}\frac{1}{a^2+b^2\cos^2\phi}\right],\end{aligned}$$

where

$$a^2 = [\zeta_{01}^2-k^2x^2-(1-\beta^2)k^2(1-x^2)]^2+4\beta^2k^4x^2(1-x^2)+4\zeta_{01}^2k^2x^2,$$

and

$$b^2 = 4\zeta_{01}^2k^2(1-x^2).$$

Integrating over azimuthal angle, ϕ, we have:

$$\frac{1}{V_0} = \frac{1}{(2\pi)^2}\int_{-1}^{1}dx\int_0^{\Lambda}dk\left\{\frac{k^2}{2\zeta_{01}^2}\left[1-\frac{a}{\sqrt{a^2+b^2}}\right]+\frac{k^2(k^2x^2+\zeta_{01}^2-(1-\beta^2)(1-x^2)k^2)}{a\sqrt{a^2+b^2}}\right\}.$$

Expand the integrand for small ζ_{01}, then as $\zeta_{01}\to 0$, the first term gives a contribution proportional to Λ, and the second gives a Λ independent contribution from $\delta(k)$. Keeping terms proportional to Λ.

$$\frac{1}{V_{01}} = \frac{\Lambda}{2\pi^2}\int_0^1 dx\frac{\beta^2+(1-\beta^2)x^2}{[x^2+(1-\beta^2)(1-x^2)]^2+4\beta^2x^2(1-x^2)}.$$

We can write the denominator in the form $\beta^2(\beta^2-4)(x^2-\gamma_+)(x^2+\gamma_-)$, where

$$\gamma_+ = \frac{(\beta^2-3)}{(\beta^2-4)}+\sqrt{\frac{(\beta^2-3)^2}{(\beta^2-4)^2}+\frac{(1-\beta^2)^2}{\beta^2(4-\beta^2)}},$$

and

$$\gamma_- = -\frac{(\beta^2-3)}{(\beta^2-4)} + \sqrt{\frac{(\beta^2-3)^2}{(\beta^2-4)^2} + \frac{(1-\beta^2)^2}{\beta^2(4-\beta^2)}}.$$

[Note: for $0 < \beta < 1$, $\gamma_\pm$ are both greater than zero.]

Thus, we have:

$$\frac{1}{V_{01}} = \frac{\Lambda}{2\pi^2}\frac{1}{\beta^2(\beta^2-4)}\frac{1}{(\gamma_+ + \gamma_-)}\left\{\frac{\beta^2+(1-\beta^2)\gamma_+}{2\sqrt{\gamma_+}}\ln\left|\frac{1-\sqrt{\gamma_+}}{1+\sqrt{\gamma_+}}\right| - \frac{\beta^2-(1-\beta^2)\gamma_-}{\sqrt{\gamma_-}}\tan^{-1}\frac{1}{\sqrt{\gamma_-}}\right\}.$$

For the case of ζ_{02}, the integral over azimuthal angle gives the same result as in the case of ζ_{01}, hence the critical coupling $V_{01} = V_{02}$. The overlap between the results for the order parameters ζ_{01} and ζ_{02} has roots in the symmetry in the Hamiltonian. As we see next, this symmetry also results in a common expression for the couplings V_3 and V_5 for the order parameters ζ_3 and ζ_5.

The equation for the order parameter associated with ζ_3 is:

$$\frac{\zeta_3}{V_3} = \int\frac{dk_x}{2\pi}\frac{dk_y}{2\pi}\int\frac{dk_0}{2\pi}\frac{(k_0^2+(1-\beta^2)|k|^2+\zeta_3^2+2\beta^2k_x^2)\zeta_3}{(-k_0^2-(1-\beta^2)|k|^2-\zeta_3^2)^2+4\beta^2(k_0^2|k|^2+\zeta_3^2k_x^2)}.$$

The integral to be solved is then:

$$\frac{1}{V_3} = \frac{1}{(2\pi)^3}\int_{-1}^{1}dx\int_0^\Lambda k^2dk\int_0^{2\pi}d\phi\left\{\frac{(k^2x^2+\zeta_3^2+(1-\beta^2)(1-x^2)k^2)}{a^2+b^2\cos^2\phi} + \frac{2\beta^2k^2(1-x^2)\cos^2\phi}{a^2+b^2\cos^2\phi}\right\},$$

where

$$a^2 = (k^2x^2+\zeta_3^2+(1-\beta^2)(1-x^2)k^2)^2+4\beta^2k^4x^2(1-x^2),$$

and

$$b^2 = 4\beta^2\zeta_3^2k^2(1-x^2).$$

The integrals over azimuthal angle, ϕ, may be evaluated using

$$\int_0^{2\pi}d\phi\frac{\cos^2\phi}{a^2+b^2\cos^2\phi} = 2\pi\left(\frac{1}{b^2} - \frac{a}{b^2\sqrt{a^2+b^2}}\right),$$

and

$$\int_0^{2\pi}d\phi\frac{1}{a^2+b^2\cos^2\phi} = \frac{2\pi}{a\sqrt{a^2+b^2}}.$$

Thus,

$$\frac{1}{V_3} = \frac{1}{(2\pi)^2}\int_{-1}^{1} dx \int_0^{\Lambda} k^2 dk \left\{ \frac{(k^2x^2+\zeta_3^2+(1-\beta^2)(1-x^2)k^2)}{a\sqrt{a^2+b^2}} + \frac{2\beta^2k^2(1-x^2)}{b^2}\left[1-\frac{a}{\sqrt{a^2+b^2}}\right]\right\}.$$

Keeping lowest order terms in ζ_3 and taking the limit $\zeta_3 \to 0$, we determine that

$$\frac{1}{V_3} = \frac{\Lambda}{2\pi^2}\frac{1}{\beta^2(\beta^2-4)}\frac{1}{(\gamma_+ + \gamma_-)}\left\{\frac{1}{2\sqrt{\gamma_+}}\ln\left|\frac{1-\sqrt{\gamma_+}}{1+\sqrt{\gamma_+}}\right| - \frac{1}{\sqrt{\gamma_-}}\tan^{-1}\frac{1}{\sqrt{\gamma_-}}\right\},$$

where $\gamma_\pm$ were defined previously.
For ζ_5, we have:

$$\frac{\zeta_5}{V_5} = \int \frac{dk_x}{2\pi}\frac{dk_y}{2\pi}\int \frac{dk_0}{2\pi}\frac{(k_0^2+(1-\beta^2)|k|^2+\zeta_5^2+2\beta^2k_y^2)\zeta_5}{(-k_0^2-(1-\beta^2)|k|^2-\zeta_5^2)^2+4\beta^2(k_0^2|k|^2+\zeta_5^2k_y^2)},$$

which leads to the same result as for ζ_3.

There are four other order parameters that arise for the Fock channel. The saddle point equations for ζ_1, ζ_2, ζ_{03} and ζ_{05} all lead to solutions that vanish identically.

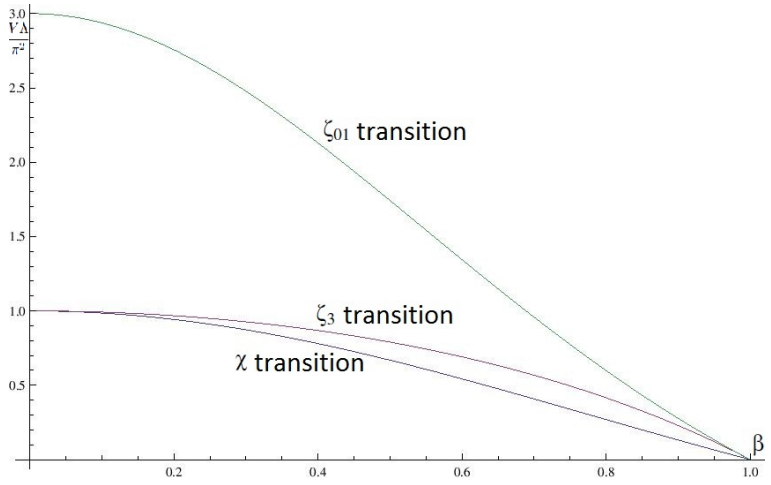

Figure 4.1: Competition between the order parameters of the Hartree channel, χ, and that of the Fock channel, ζ_{01} and ζ_3.

A comparision of the plots of the critical couplings for the Hartree channel, χ, and the Fock channels, ζ_{01} and ζ_3 that is depicted in Fig. 4.1 shows that the critical couplings for the

Hartree channel, χ, is more sensitive than ζ_{01} of the Fock channel. On close examination of Fig. 4.1, we see that for $0 < \beta < 1$, $V_\chi < V_3 < V_{01}$, so for $\beta \neq 0, 1$ the leading stability is to a charge density wave. When $\beta = 1$, there is a flat band and the analysis here is insufficient to discriminate between correlated states. For $\beta = 0$, $V_\chi = V_3$ (as shown more clearly in Fig. 4.2) and so we need to consider both orders simultaneously to discriminate between them.

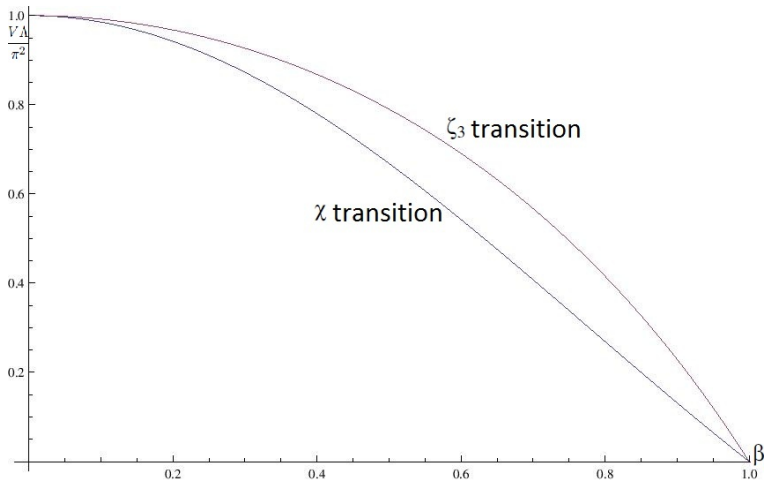

Figure 4.2: Competition between the order parameters of the Hartree channel, χ, and one of the Fock channels, ζ_3.

Now, consider the situation in which both χ and ζ_3 may be non-zero. Then

$$\frac{4\chi}{V_0} = \mathrm{Tr}(M^{-1}),$$

and

$$\frac{4\zeta_3}{V_0} = \mathrm{Tr}(i\gamma_3 M^{-1})$$

are the saddle point equations to be satisfied and M includes both χ and ζ_3:

$$M = \chi I + i\gamma_0 k_0 + i\gamma_1 k_1 + i\gamma_2 k_2 + \zeta_3 i\gamma_3 - \beta k_1 \gamma_0 \gamma_3 - \beta k_2 \gamma_0 \gamma_5.$$

We need to solve $MM^{-1} = I$, i.e.

$$\{\chi I + i\gamma_0 k_0 + i\gamma_1 k_1 + i\gamma_2 k_2 - \beta k_1 \gamma_0 \gamma_3 - \beta k_2 \gamma_0 \gamma_5 + \zeta_3 i\gamma_3\} M^{-1} = I.$$

Hence we have:

$$\frac{\chi}{V_0} = \chi \int \frac{d^3k}{(2\pi)^3} \frac{1}{A'} \left[\chi^2 + \zeta_3^2 + k_0^2 + (1+\beta^2)|\vec{k}|^2 \right], \tag{4.12}$$

and

$$\frac{\zeta_3}{V_0} = \zeta_3 \int \frac{d^3k}{(2\pi)^3} \frac{1}{A'} \left[\chi^2 + k_0^2 + (1-\beta^2)|\vec{k}|^2 + 2\beta^2 k_1^2 + \zeta_3^2 \right], \tag{4.13}$$

where

$$A' = \left[\chi^2 - \zeta_3^2 - k_0^2 - (1-\beta^2)|\vec{k}|^2 \right]^2 + 4\beta^2 k_0^2 |\vec{k}|^2 + 4\chi^2 (k_0^2 + |\vec{k}|^2) + 4\beta^2 k_1^2 \zeta_3^2 + 4\chi^2 \zeta_3^2.$$

Now, if $\chi \neq 0$, then we can combine Eqs 4.12 and 4.13 to write:

$$\frac{\zeta_3}{V_0} = \frac{\zeta_3}{\chi} \frac{\chi}{V_0} - \zeta_3 \int \frac{d^3k}{(2\pi)^3} \frac{2\beta^2 k_2^2}{A'}. \tag{4.14}$$

The only solution to this equation is $\zeta_3 = 0$, since the integral on the right-hand-side is always positive. Hence, it is not possible to have coexistence of ζ_3 and χ order for $\beta \neq 0$. We now focus on $\beta = 0$ and consider the situation where $\zeta_3 \neq 0$, $\chi \to 0$ and determine V_χ. From above,

$$\frac{1}{V_0} = \frac{1}{8\pi^3} \int_0^{2\pi} d\phi \int_{-1}^{1} dx \int_0^{\Lambda} dk \frac{k^2 [\zeta_3^2 + k^2 x^2 + k^2 (1-x^2)]}{[k^2 x^2 + k^2 (1-x^2) + \zeta_3^2]^2}, \tag{4.15}$$

which leads to

$$\begin{aligned} \frac{1}{V_\chi} &= \frac{1}{4\pi^2} \int_{-1}^{1} dx \int_0^{\Lambda} dk \frac{k^2}{[k^2 + \zeta_3^2]} \\ &= \frac{1}{2\pi^2} \int_0^{\Lambda} dk \left[1 - \frac{\zeta_3^2}{[k^2 + \zeta_3^2]} \right] \\ &= \frac{\Lambda}{2\pi^2} - \frac{1}{\zeta_3} \tan^{-1} \left(\frac{\Lambda}{\zeta_3} \right) \end{aligned}$$

Similarly, when $\beta = 0$ and we take $\chi \neq 0$, $\zeta_3 \to 0$, we find

$$\frac{1}{V_3} = \frac{\Lambda}{2\pi^2} - \frac{1}{\chi} \tan^{-1} \left(\frac{\Lambda}{\chi} \right).$$

Hence, we are not able, at the level of our analysis to determine whether charge density wave ordering from χ or ζ_3 (or ζ_5, recalling they are equivalent) ordering, which corresponds to circulating currents

$$\zeta_3 \propto -\frac{i}{4}\left[\left\langle \psi_A^\dagger \psi_C \right\rangle - \left\langle \psi_C^\dagger \psi_A \right\rangle - \left\langle \psi_B^\dagger \psi_D \right\rangle + \left\langle \psi_D^\dagger \psi_B \right\rangle\right],$$

and

$$\zeta_5 \propto -\frac{i}{4}\left[\left\langle \psi_A^\dagger \psi_B \right\rangle - \left\langle \psi_B^\dagger \psi_A \right\rangle + \left\langle \psi_C^\dagger \psi_D \right\rangle - \left\langle \psi_D^\dagger \psi_C \right\rangle\right],$$

wins out at $\beta = 0$. Given that the Hartree term wins out for any finite β, we suspect that it also wins out at $\beta = 0$. Moreover, we expect the degeneracy to be lifted by keeping higher order terms in momentum expansion.

4.1.2 Symmetry Relations between Order Parameters

It is important to appreciate the additional discrete symmetry in the Hamiltonian H_k, which holds even when $\beta \neq 0$, that we defined in Chapter 3:

$$\Gamma = \frac{i}{2}(\gamma_2\gamma_3 + \gamma_1\gamma_5) - \frac{i}{2}(\gamma_1\gamma_3 + \gamma_2\gamma_5).$$

The effect of Γ on various gamma matrix combinations is as follows:

$$\begin{aligned} \Gamma\gamma_3\Gamma^{-1} &= \gamma_5; \qquad \Gamma\gamma_5\Gamma^{-1} = \gamma_3, \\ \Gamma\gamma_0\gamma_1\Gamma^{-1} &= \gamma_0\gamma_2; \qquad \Gamma\gamma_0\gamma_2\Gamma^{-1} = \gamma_0\gamma_1. \end{aligned}$$

This illustrates why the action of Γ on H_k is to exchange k_x and k_y. It also illustrates that the order parameter pairs ζ_3, ζ_5 and ζ_{01}, ζ_{02} should have the same critical coupling since they can be transformed into each other.

4.2 Next Nearest Neighbour Interactions

In addition to nearest neighbour interactions, we now consider next-nearest neighbour interations,

$$\hat{H}_{\text{int}} = U_0 \sum_{\ll i,j \gg} \hat{n}_i \hat{n}_j,$$

where we assume the strength of the interaction is the same for all neighbours and $\ll i, j \gg$ indicates that i and j are next nearest neighbours. This leads to a contribution to the Lagrangian in the low energy limit of

$$\mathcal{L}_{\text{nnn}} = -4U_0 \sum_{\vec{r}} \left\{ \psi_A^\dagger(\vec{r})\psi_A(\vec{r})\psi_D^\dagger(\vec{r})\psi_D(\vec{r}) + \psi_B^\dagger(\vec{r})\psi_B(\vec{r})\psi_C^\dagger(\vec{r})\psi_C(\vec{r}) \right\}. \tag{4.16}$$

We can decompose this interaction term into Hartree and Fock parts as follows:

$$\begin{aligned} &\left\langle \psi_A^\dagger \psi_A \right\rangle \psi_D^\dagger \psi_D + \psi_A^\dagger \psi_A \left\langle \psi_D^\dagger \psi_D \right\rangle + \left\langle \psi_B^\dagger \psi_B \right\rangle \psi_C^\dagger \psi_C + \psi_B^\dagger \psi_B \left\langle \psi_C^\dagger \psi_C \right\rangle \\ &-\psi_A^\dagger \left\langle \psi_D^\dagger \psi_A \right\rangle \psi_D - \psi_D^\dagger \left\langle \psi_A^\dagger \psi_D \right\rangle \psi_A - \psi_B^\dagger \left\langle \psi_C^\dagger \psi_B \right\rangle \psi_C - \psi_C^\dagger \left\langle \psi_B^\dagger \psi_C \right\rangle \psi_B. \end{aligned}$$

Writing this in the form:

$$\psi^\dagger N \psi = \bar{\psi}\gamma_0 N \psi,$$

gives:

$$N = \begin{pmatrix} <\psi_D^\dagger \psi_D> & 0 & 0 & -<\psi_D^\dagger \psi_A> \\ 0 & <\psi_C^\dagger \psi_C> & -<\psi_C^\dagger \psi_B> & 0 \\ 0 & -<\psi_B^\dagger \psi_C> & <\psi_B^\dagger \psi_B> & 0 \\ -<\psi_A^\dagger \psi_D> & 0 & 0 & <\psi_A^\dagger \psi_A> \end{pmatrix}.$$

Recall the definitions

$$\gamma_0 = \begin{pmatrix} \sigma_0 & 0 \\ 0 & -\sigma_0 \end{pmatrix}, i\gamma_1\gamma_3 = \begin{pmatrix} -I_2 & 0 \\ 0 & I_2 \end{pmatrix}, i\gamma_2\gamma_5 = \begin{pmatrix} -\sigma_3 & 0 \\ 0 & -\sigma_3 \end{pmatrix}, i\gamma_1\gamma_2 = \begin{pmatrix} 0 & -\sigma_2 \\ -\sigma_2 & 0 \end{pmatrix},$$

$$i\gamma_3\gamma_5 = \begin{pmatrix} 0 & -i\sigma_1 \\ i\sigma_1 & 0 \end{pmatrix}, i\gamma_2\gamma_3 = \begin{pmatrix} 0 & -i\sigma_2 \\ i\sigma_2 & 0 \end{pmatrix}, i\gamma_1\gamma_5 = \begin{pmatrix} 0 & \sigma_1 \\ \sigma_1 & 0 \end{pmatrix}.$$

We can then see that $\bar{\psi}(\gamma_0 N)\psi$ takes the form

$$\bar{\psi}\left\{\delta_0\gamma_0 + m_0 I_4 + \zeta_{13}(i\gamma_1\gamma_3) + \zeta_{25}(i\gamma_2\gamma_5) + \zeta_{15}(i\gamma_1\gamma_5) + \zeta_{23}(i\gamma_2\gamma_3) + \zeta_{35}(i\gamma_3\gamma_5) + \zeta_{12}(i\gamma_1\gamma_2)\right\}\psi,$$

where δ_0 and m_0 are the chemical potential shift and the charge density wave ordering we had for the nearest neighbour interactions in Sec. 4.1, respectively. The additional Hartree

terms

$$\begin{aligned}\zeta_{13} &\propto (n_A - n_B + n_C - n_D),\\ \zeta_{25} &\propto (n_A + n_B - n_C - n_D),\end{aligned}$$

correspond to broken rotation by $\pi/2$ symmetry, which can be related to the staggered potentials introduced in Chapter 3. Namely, ζ_{13} corresponds to $\Delta_2 + \Delta_3$ and ζ_{25} corresponds to $\Delta_2 - \Delta_3$ for the staggered potentials illustrated in Fig. 3.6. The Fock terms correspond to next-nearest neighbour hopping:

$$\begin{aligned}\zeta_{15} &\propto -\left[\left\langle \psi_A^\dagger \psi_D \right\rangle + \left\langle \psi_D^\dagger \psi_A \right\rangle - \left\langle \psi_B^\dagger \psi_C \right\rangle - \left\langle \psi_C^\dagger \psi_B \right\rangle\right],\\ \zeta_{23} &\propto \left[\left\langle \psi_A^\dagger \psi_D \right\rangle + \left\langle \psi_D^\dagger \psi_A \right\rangle + \left\langle \psi_B^\dagger \psi_C \right\rangle + \left\langle \psi_C^\dagger \psi_B \right\rangle\right],\\ \zeta_{35} &\propto \frac{1}{i}\left[\left\langle \psi_A^\dagger \psi_D \right\rangle - \left\langle \psi_D^\dagger \psi_A \right\rangle - \left\langle \psi_B^\dagger \psi_C \right\rangle + \left\langle \psi_C^\dagger \psi_B \right\rangle\right],\\ \zeta_{12} &\propto -\frac{1}{i}\left[\left\langle \psi_A^\dagger \psi_D \right\rangle - \left\langle \psi_D^\dagger \psi_A \right\rangle + \left\langle \psi_B^\dagger \psi_C \right\rangle - \left\langle \psi_C^\dagger \psi_B \right\rangle\right],\end{aligned}$$

The parameters ζ_{15} and ζ_{23} generate real next-nearest neighbour hopping and at the mean-field level, ζ_{35} and ζ_{12} correspond to imaginary next-nearest neighbour hopping, as is illustrated for ζ_{35} for the A and D sites for hopping amplitude α in Fig. 4.3 (there will also be similar hopping between B and C sites). Such hopping leads to a term $i\alpha \sin(k_x a)\sin(k_y a)$ in the Hamiltonian H_k.

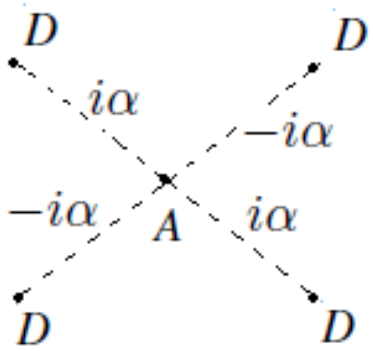

Figure 4.3: Imaginary next-nearest neighbour hopping for ζ_{35} for the A and D sites for hopping amplitude α.

In order to incorporate these terms into the path integral, it is useful to note that the Hartree terms correspond to the decomposition.

$$\begin{aligned} n_A n_D + n_B n_C &= \frac{1}{8}[(n_A+n_B+n_C-n_D)^2+(n_A-n_B-n_C+n_D)^2-(n_A-n_B+n_C-n_D)^2 \\ &\quad -(n_A+n_B-n_C-n_D)^2] \\ &= \frac{1}{8}\left[(\bar{\psi}\gamma_0\psi)^2+(\bar{\psi}\psi)^2-(\bar{\psi}i\gamma_1\gamma_3\psi)^2-(\bar{\psi}i\gamma_2\gamma_5\psi)^2\right], \end{aligned}$$

and the Fock terms to

$$n_A n_D + n_B n_C = -\frac{1}{8}\left[(\bar{\psi}i\gamma_1\gamma_5\psi)^2+(\bar{\psi}i\gamma_2\gamma_3\psi)^2+(\bar{\psi}i\gamma_3\gamma_5\psi)^2+(\bar{\psi}i\gamma_1\gamma_2\psi)^2\right].$$

Using this knowledge, we can decouple the interaction term in the action by introducing an additional 6 Hubbard-Stratonovich fields: ζ_{13}, ζ_{25}, ζ_{15}, ζ_{23}, ζ_{35} and ζ_{12}. This will lead to 6 additional terms in S_{mix}

$$\begin{aligned} S_{\text{mix}} &= \int_0^\beta d\tau \int d^2\vec{x}\{\zeta_{13}\bar{\psi}i\gamma_1\gamma_3\psi+\zeta_{25}\bar{\psi}i\gamma_2\gamma_5\psi+\zeta_{15}\bar{\psi}i\gamma_1\gamma_5\psi \\ &\quad +\zeta_{23}\bar{\psi}i\gamma_2\gamma_3\psi+\zeta_{35}\bar{\psi}i\gamma_3\gamma_5\psi+\zeta_{12}\bar{\psi}i\gamma_1\gamma_2\psi\}, \end{aligned}$$

with additional terms in the action for each of the new fields ζ_i

$$S[\zeta_i] = \frac{2}{U_0}\int_0^\beta d\tau \int d^2\vec{x}\,[\zeta_i(\vec{x},\tau)]^2.$$

The actions for χ and ϕ are modified to:

$$S[\chi] = \frac{2}{V_0 - U_0} \int_0^\beta d\tau \int d^2\vec{x}\,[\chi(\vec{x},\tau)]^2\,,$$

provided $V_0 > U_0$, and

$$S[\phi] = \frac{2}{V_0 + U_0} \int_0^\beta d\tau \int d^2\vec{x}\,[\phi(\vec{x},\tau)]^2\,.$$

The *saddle point* equations become:

$$\begin{aligned}
\frac{4\chi}{V_0 - U_0} &= \mathrm{tr}(M^{-1}), \\
\frac{4\phi}{V_0} &= \mathrm{tr}(i\gamma_0 M^{-1}), \\
\frac{4\zeta_i}{V_0} &= \mathrm{tr}(\Gamma_i M^{-1}), \qquad \text{for } \Gamma_i \in \{\gamma_0\gamma_1, i\gamma_1, \gamma_0\gamma_3, i\gamma_3, \gamma_0\gamma_2, i\gamma_2, \gamma_0\gamma_5, i\gamma_5\}\,, \\
\frac{4\zeta_i}{U_0} &= \mathrm{tr}(\Gamma_i M^{-1}), \qquad \text{for } \Gamma_i \in \{i\gamma_1\gamma_3, i\gamma_2\gamma_5, i\gamma_1\gamma_5, i\gamma_2\gamma_3, i\gamma_3\gamma_5, i\gamma_1\gamma_2\}\,.
\end{aligned} \tag{4.17}$$

As before, we investigate the transitions for each of the new order parameters separately initially, by setting all other order parameters to zero and focusing only on one saddle point equation. We now calculate the appropriate M^{-1} for each of these order parameters.

For ζ_{13}:

$$M = ik_0\gamma_0 + ik_1\gamma_1 + ik_2\gamma_2 - \beta k_1\gamma_0\gamma_3 - \beta k_2\gamma_0\gamma_5 + i\zeta_{13}\gamma_1\gamma_3,$$

hence,

$$\begin{aligned}
M^{-1} &= \frac{1}{A}\left\{\left[-k_0^2 - (1-\beta^2)|\vec{k}|^2 - \zeta_{13}^2\right] I - 2i\beta k_2\zeta_{13}\gamma_2 + 2ik_1(\beta k_0 - i\zeta_{13})\gamma_3 + 2i\beta k_0 k_2\gamma_5\right\} \\
&\times \{ik_0\gamma_0 + ik_1\gamma_1 + ik_2\gamma_2 + \beta k_1\gamma_0\gamma_3 + \beta k_2\gamma_0\gamma_5 - i\zeta_{13}\gamma_1\gamma_3\}\,,
\end{aligned}$$

with

$$A = \left[-k_0^2 - (1-\beta^2)|\vec{k}|^2 - \zeta_{13}^2\right]^2 + 4\beta^2 k_0^2|\vec{k}|^2 - 4(k_1^2 - \beta^2 k_2^2)\zeta_{13}^2 - 8i\beta k_0 k_1^2\zeta_{13}.$$

For ζ_{25}:

$$M = ik_0\gamma_0 + ik_1\gamma_1 + ik_2\gamma_2 - \beta k_1\gamma_0\gamma_3 - \beta k_2\gamma_0\gamma_5 + i\zeta_{25}\gamma_2\gamma_5,$$

hence,

$$\begin{aligned} M^{-1} &= \frac{1}{A}\left\{\left[-k_0^2 - (1-\beta^2)|\vec{k}|^2 - \zeta_{25}^2\right]^2 I - 2i\beta k_1\zeta_{25}\gamma_1 + 2i\beta k_0 k_1\gamma_3 + 2ik_2(\beta k_0 - i\zeta_{25})\gamma_5\right\} \\ &\quad \times \left\{ik_0\gamma_0 + ik_1\gamma_1 + ik_2\gamma_2 + \beta k_1\gamma_0\gamma_3 + \beta k_2\gamma_0\gamma_5 - i\zeta_{25}\gamma_2\gamma_5\right\}, \end{aligned}$$

with

$$A = \left[-k_0^2 - (1-\beta^2)|\vec{k}|^2 - \zeta_{25}^2\right]^2 + 4\beta^2 k_0^2|\vec{k}|^2 - 4(\beta^2 k_1^2 - k_2^2)\zeta_{25}^2 - 8i\beta k_0 k_2^2\zeta_{25}.$$

For ζ_{15}:

$$M = ik_0\gamma_0 + ik_1\gamma_1 + ik_2\gamma_2 - \beta k_1\gamma_0\gamma_3 - \beta k_2\gamma_0\gamma_5 + i\zeta_{15}\gamma_1\gamma_5,$$

hence,

$$\begin{aligned} M^{-1} &= \frac{1}{A}\left\{\left[-k_0^2 - (1-\beta^2)|\vec{k}|^2 - \zeta_{15}^2\right] I + 2i\beta k_1\zeta_{15}\gamma_2 + 2i(\beta k_0 k_2 - ik_1\zeta_{15})\gamma_5 + 2i\beta k_0 k_1\gamma_3\right\} \\ &\quad \times \left\{ik_0\gamma_0 + ik_1\gamma_1 + ik_2\gamma_2 + \beta k_1\gamma_0\gamma_3 + \beta k_2\gamma_0\gamma_5 - i\zeta_{15}\gamma_1\gamma_5\right\}, \end{aligned}$$

with

$$A = \left[-k_0^2 - (1-\beta^2)|\vec{k}|^2 - \zeta_{15}^2\right]^2 + 4\beta^2 k_0^2|\vec{k}|^2 - 4(1-\beta^2)k_1^2\zeta_{15}^2 - 8i\beta k_0 k_1 k_2\zeta_{15}.$$

For ζ_{23}:

$$M = ik_0\gamma_0 + ik_1\gamma_1 + ik_2\gamma_2 - \beta k_1\gamma_0\gamma_3 - \beta k_2\gamma_0\gamma_5 + \zeta_{23}i\gamma_2\gamma_3,$$

hence,

$$\begin{aligned} M^{-1} &= \frac{1}{A}\left\{\left[-k_0^2 - (1-\beta^2)|\vec{k}|^2 - \zeta_{23}^2\right] I + 2i\beta k_2\zeta_{23}\gamma_1 + 2i(\beta k_0 k_1 - ik_2\zeta_{23})\gamma_3 + 2i\beta k_0 k_2\gamma_5\right\} \\ &\quad \times \left\{ik_0\gamma_0 + ik_1\gamma_1 + ik_2\gamma_2 + \beta k_1\gamma_0\gamma_3 + \beta k_2\gamma_0\gamma_5 - \zeta_{23}i\gamma_2\gamma_3\right\}, \end{aligned}$$

with

$$A = \left[-k_0^2 - (1-\beta^2)|\vec{k}|^2 - \zeta_{23}^2\right]^2 + 4\beta^2 k_0^2|\vec{k}|^2 - 4(1-\beta^2)|\vec{k}|^2\zeta_{23}^2 - 8i\beta k_0 k_1 k_2\zeta_{23}.$$

For ζ_{35}:

$$M = ik_0\gamma_0 + ik_1\gamma_1 + ik_2\gamma_2 - \beta k_1\gamma_0\gamma_3 - \beta k_2\gamma_0\gamma_5 + \zeta_{35} i\gamma_3\gamma_5,$$

hence,

$$\begin{aligned} M^{-1} &= \frac{1}{A}\left\{\left[-k_0^2 - (1-\beta^2)|\vec{k}|^2 - \zeta_{35}^2\right] I + 2i\beta k_0 k_1 \gamma_3 + 2i\beta k_0 k_2 \gamma_5\right\} \\ &\quad \times \{ik_0\gamma_0 + ik_1\gamma_1 + ik_2\gamma_2 + \beta k_1\gamma_0\gamma_3 + \beta k_2\gamma_0\gamma_5 - \zeta_{35} i\gamma_3\gamma_5\}, \end{aligned}$$

with

$$A = \left[-k_0^2 - (1-\beta^2)|\vec{k}|^2 - \zeta_{35}^2\right]^2 + 4\beta^2 k_0^2 |\vec{k}|^2.$$

For ζ_{12}:

$$M = ik_0\gamma_0 + ik_1\gamma_1 + ik_2\gamma_2 - \beta k_1\gamma_0\gamma_3 - \beta k_2\gamma_0\gamma_5 + \zeta_{12} i\gamma_1\gamma_2,$$

hence,

$$\begin{aligned} M^{-1} &= \frac{1}{A}\{\left[-k_0^2 - (1-\beta^2)|\vec{k}|^2 - \zeta_{12}^2\right] I - 2k_2\zeta_{12}\gamma_1 + 2k_1\zeta_{12}\gamma_2 + 2i\beta(k_0 k_1 + k_2\zeta_{12})\gamma_3 \\ &\quad + 2i\beta(k_0 k_2 - k_1\zeta_{12})\gamma_5\}\{ik_0\gamma_0 + ik_1\gamma_1 + ik_2\gamma_2 + \beta k_1\gamma_0\gamma_3 + \beta k_2\gamma_0\gamma_5 - \zeta_{12} i\gamma_1\gamma_2\}, \end{aligned}$$

with

$$A = \left[-k_0^2 - (1-\beta^2)|\vec{k}|^2 - \zeta_{12}^2\right]^2 + 4\beta^2 k_0^2 |\vec{k}|^2 - 4(1-\beta^2)|\vec{k}|^2 \zeta_{12}^2.$$

Having these results for the inverse propagators in hand, we now turn to the resulting six saddle point equations:

$$\begin{aligned} \frac{4\zeta_{13}}{U_0} &= \mathrm{tr}(i\gamma_1\gamma_3 M^{-1}) \\ &= 4\int \frac{d^3\vec{k}}{(2\pi)^3} \frac{\zeta_{13}\left\{\left[k_0^2 + (1-\beta^2)|\vec{k}|^2 + \zeta_{13}^2\right] - 2(k_1^2 - \beta^2 k_2^2)\right\} - 2i\beta k_0 k_1^2}{\left[k_0^2 + (1-\beta^2)|\vec{k}|^2 + \zeta_{13}^2\right]^2 + 4\beta^2 k_0^2|\vec{k}|^2 - 4(k_1^2 - \beta^2 k_2^2)\zeta_{13}^2 - 8i\beta k_0 k_1^2 \beta\zeta_{13}}, \end{aligned}$$

$$\begin{aligned} \frac{4\zeta_{25}}{U_0} &= \mathrm{tr}(i\gamma_2\gamma_5 M^{-1}) \\ &= 4\int \frac{d^3\vec{k}}{(2\pi)^3} \frac{\zeta_{25}\left\{\left[k_0^2 + (1-\beta^2)|\vec{k}|^2 + \zeta_{25}^2\right] + 2(\beta^2 k_1^2 - k_2^2)\right\} - 2i\beta k_0 k_2^2}{\left[k_0^2 + (1-\beta^2)|\vec{k}|^2 + \zeta_{23}^2\right]^2 + 4\beta^2 k_0^2|\vec{k}|^2 + 4(\beta^2 k_1^2 - k_2^2)\zeta_{25}^2 - 8i\beta k_0 k_2^2 \beta\zeta_{25}}, \end{aligned}$$

$$\begin{aligned}\frac{4\zeta_{15}}{U_0} &= \mathrm{tr}(i\gamma_1\gamma_5 M^{-1}) \\ &= 4\int \frac{d^3\vec{k}}{(2\pi)^3}\frac{\zeta_{15}\left\{\left[k_0^2+(1-\beta^2)|\vec{k}|^2+\zeta_{15}^2\right]-2(1-\beta^2)k_1^2\right\}-2i\beta k_0k_1k_2}{\left[k_0^2+(1-\beta^2)|\vec{k}|^2+\zeta_{15}^2\right]^2+4\beta^2k_0^2|\vec{k}|^2-4(1-\beta^2)k_1^2\zeta_{15}^2-8i\beta k_0k_1k_2\zeta_{15}},\end{aligned}$$

$$\begin{aligned}\frac{4\zeta_{23}}{U_0} &= \mathrm{tr}(i\gamma_2\gamma_3 M^{-1}) \\ &= 4\int \frac{d^3\vec{k}}{(2\pi)^3}\frac{\zeta_{23}\left\{k_0^2+(1-\beta^2)|\vec{k}|^2+\zeta_{23}^2-2(1-\beta^2)k_2^2\right\}-2i\beta k_0k_1k_2}{\left[k_0^2+(1-\beta^2)|\vec{k}|^2+\zeta_{23}^2\right]^2+4\beta^2k_0^2|\vec{k}|^2-4(1-\beta^2)k_2^2\zeta_{23}^2-8i\beta k_0k_1k_2\zeta_{23}},\end{aligned}$$

$$\begin{aligned}\frac{4\zeta_{35}}{U_0} &= \mathrm{tr}(i\gamma_3\gamma_5 M^{-1}) \\ &= 4\zeta_{35}\int \frac{d^3\vec{k}}{(2\pi)^3}\frac{k_0^2+(1-\beta^2)|\vec{k}|^2+\zeta_{35}^2}{\left[k_0^2+(1-\beta^2)|\vec{k}|^2+\zeta_{35}^2\right]^2+4\beta^2k_0^2|\vec{k}|^2},\end{aligned}$$

and

$$\begin{aligned}\frac{4\zeta_{12}}{U_0} &= \mathrm{tr}(i\gamma_1\gamma_2 M^{-1}) \\ &= 4\zeta_{12}\int \frac{d^3\vec{k}}{(2\pi)^3}\frac{k_0^2-(1-\beta^2)|\vec{k}|^2+\zeta_{12}^2}{\left[k_0^2+(1-\beta^2)|\vec{k}|^2+\zeta_{12}^2\right]^2+4\beta^2k_0^2|\vec{k}|^2-4(1-\beta^2)|\vec{k}|^2\zeta_{12}^2}.\end{aligned}$$

Now, we noted that the form of the saddle point equation for χ only holds if $V_0 > U_0$. If $V_0 \leq U_0$, then there will not be ordering in χ.

We now solve the saddle point equations for the critical couplings by investigating the value of U for which the order parameter vanishes.

For ζ_{13}, we find, making use of similar manipulations to the case of nearest neighbour interactions, that

$$\frac{1}{U_{13}} = \frac{\Lambda}{2\pi^2}\frac{1}{\beta^2(\beta^2-4)}\left\{\frac{\sqrt{\gamma_+}}{2}\ln\left|\frac{1-\sqrt{\gamma_+}}{1+\sqrt{\gamma_+}}\right|+\sqrt{\gamma_-}\tan^{-1}\left(\frac{1}{\sqrt{\gamma_-}}\right)\right\}.$$

We find that the gap equation for ζ_{25} is identical to that of ζ_{13} up to the transformation

$k_1 \longleftrightarrow k_2$ and $\zeta_{13} \longleftrightarrow \zeta_{25}$, hence $U_{25} = U_{13}$. Similar arguments give $U_{15} = U_{23}$ and

$$\frac{1}{U_{15}} = \frac{1}{U_{23}} = \frac{\Lambda}{2\pi^2}\frac{1}{\beta^2(\beta^2-4)}\frac{1}{(\gamma_+ + \gamma_-)}\left\{\frac{\sqrt{\gamma_+}}{2}\ln\left|\frac{1-\sqrt{\gamma_+}}{1+\sqrt{\gamma_+}}\right| + \sqrt{\gamma_-}\tan^{-1}\left(\frac{1}{\sqrt{\gamma_-}}\right)\right\}.$$

We also find

$$\frac{1}{U_{35}} = \frac{\Lambda}{2\pi^2}\frac{1}{\beta^2(\beta^2-4)}\frac{1}{(\gamma_+ + \gamma_-)}\left\{\frac{(1-\beta^2+\beta^2\gamma_+)}{2\sqrt{\gamma_+}}\ln\left|\frac{1-\sqrt{\gamma_+}}{1+\sqrt{\gamma_+}}\right| - \frac{(1-\beta^2-\beta^2\gamma_-)}{\sqrt{\gamma_-}}\tan^{-1}\left(\frac{1}{\sqrt{\gamma_-}}\right)\right\},$$

and

$$\begin{aligned}\frac{1}{U_{12}} &= \frac{\Lambda}{2\pi^2}\frac{1}{\beta^2(\beta^2-4)}\frac{1}{(\gamma_+ + \gamma_-)}\left\{\frac{(1-\beta^2+(2-\beta^2)\gamma_-)}{\sqrt{\gamma_-}}\tan^{-1}\left(\frac{1}{\sqrt{\gamma_-}}\right)\right. \\ &\quad \left. - \frac{(1-\beta^2-(2-\beta^2)\gamma_+)}{2\sqrt{\gamma_+}}\ln\left|\frac{1-\sqrt{\gamma_+}}{1+\sqrt{\gamma_+}}\right|\right\},\end{aligned}$$

where γ_+ and γ_- were defined previously.

In Fig. 4.4, we plot the critical values for each order parameter as a function of β, with the exception of U_{12}, which is always negative, as is not of interest to us here as we only consider repulsive interactions. We note that for small β, broken rotation symmetry ζ_{13} or ζ_{25} wins out, but at a critical $\beta_c \simeq 0.343$, circulating current order of the ζ_{35} becomes the favoured order. This shows an unusual feature for birefringent fermions, that in the presence of birefringence a phase that would otherwise not be favoured for regular Dirac fermions at $\beta = 0$ is stabilized at finite β.

4.3 Phase Diagrams

From our investigations of nearest neighbour and next nearest neighbour interactions, we were able to find the phase diagram of birefringent fermions as a function of nearest-neighbour interaction strength V_0 and birefringence parameter β, as illustrated in Fig. 4.5.

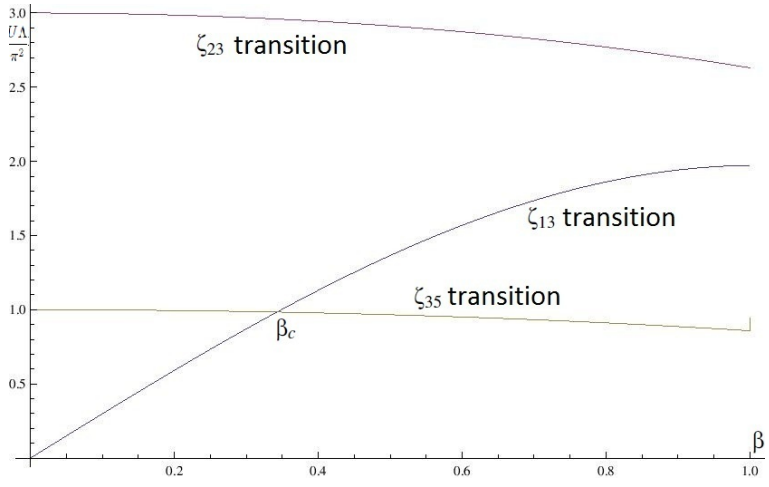

Figure 4.4: Competition between order parameters for the next-nearest neighbours in units of the cutoff versus β.

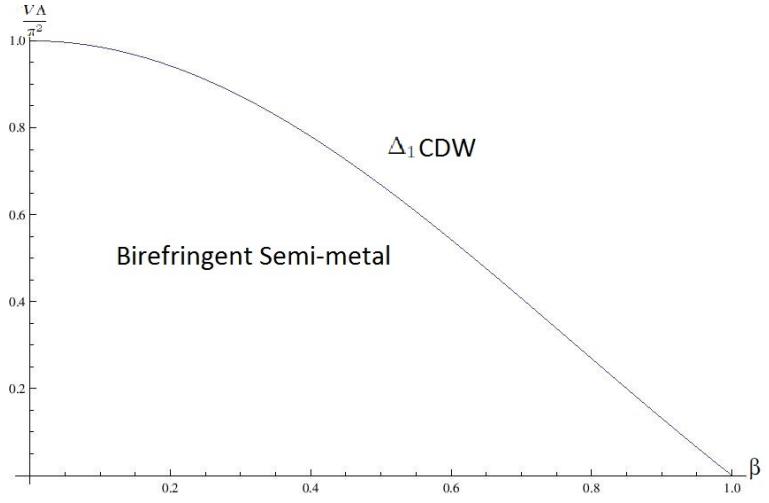

Figure 4.5: The critical potential for the Hartree channel, χ, in units of the cutoff versus β.

For next nearest interactions, the phase diagram is as illustrated in Fig. 4.6.

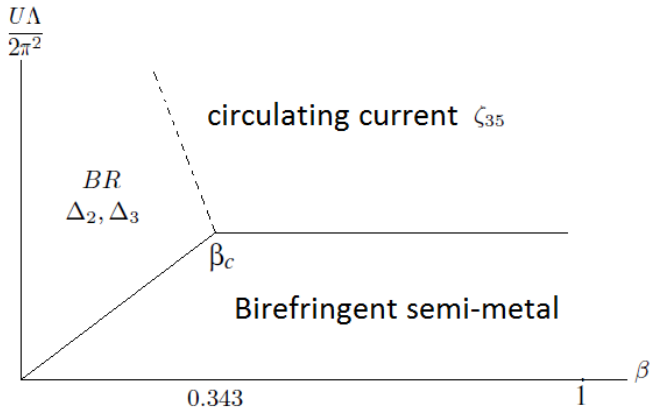

Figure 4.6: Schematic phase diagram for the next nearest neighbour interaction strength as a function of β.

We have not investigated the transition between charge density wave ordering, broken rotation symmetry and the circulating current phase. Combining the phase diagrams including nearest neighbour and next nearest neighbour interactions, we can see that these will depend on U, V and β. Fig. 4.7 shows the phase diagam at small β schematically.

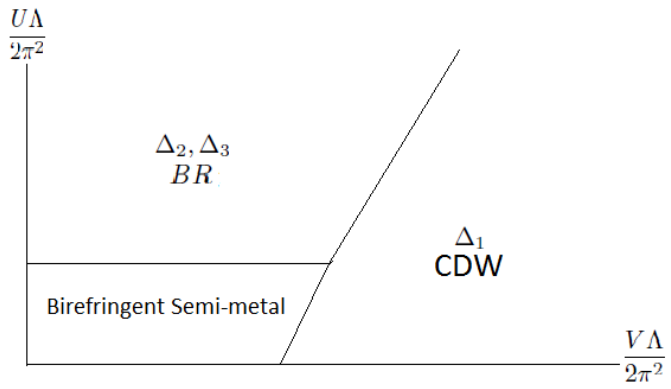

Figure 4.7: Schematic phase diagram for small β when there are both nearest neighbour and next-nearest neighbour interactions.

whilst Fig. 4.8 shows the phase diagram for larger β.

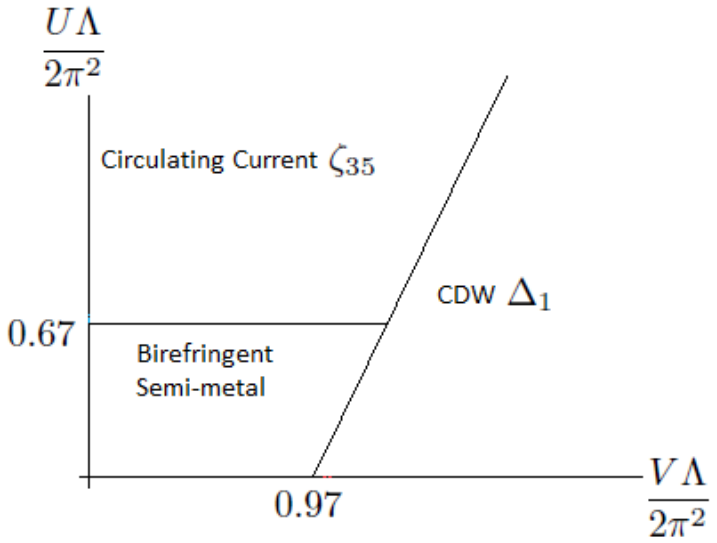

Figure 4.8: Numerically determined phase diagram for $\beta > \beta_c$, calculated at $\beta = 0.50$.

In the case of ζ_{35} and χ order, we have considered the competition between the orders when $\beta > \beta_c$ by solving the equations:

$$\frac{\chi}{V_0 - U_0} = \frac{\chi}{2\pi^2}\int_0^\Lambda dk \int_0^1 dx \frac{1}{A} k^2 \left[\chi^2 + (1+\beta^2)k^2 - \beta^2 k^2 x^2 - \zeta_{35}^2\right],$$

$$\frac{\zeta_{35}}{U_0} = \frac{\zeta_{35}}{2\pi^2}\int_0^\Lambda dk \int_0^1 \frac{1}{A} k^2 \left[-\chi^2 + (1-\beta^2)k^2 + \beta^2 k^2 x^2 + \zeta_{35}^2\right],$$

where

$$A = \left[\chi^2 - (1-\beta^2)k^2 - \beta^2 k^2 x^2 - \zeta_{35}^2\right]^2 + 4\chi^2 k^2 + 4\beta^2 k^4 x^2 (1-x^2),$$

simultaneously. The numerical solution of these equations for $\beta = 0.5$ is shown in Fig. 4.8 and solutions for larger β will be qualitatively similar.

4.4 Summary

In this chapter, we studied the effects of nearest and next-nearest interactions on birefringent fermions and saw the possible phases that can result from the interacting Hamiltonian terms. We only studied the repulsive interactions between the spinless fermions and the

calculations were done at a mean-field level but both Hartree and Fock channels were considered. We showed that for the nearest neighbour interactions, the Hartree term wins out and gives rise to charge density wave ordering. For next-nearest neighbour interactions, there is charge density wave ordering and broken rotation symmetry for small β, with a transition to circulating order at larger β. This illustrates the richness of possible phases that can arise for birefringent fermions that are not present for regular Dirac fermions, especially when there are both nearest neighbour and next-nearest neighbour interactions.

Chapter 5

Birefringent Fermions in a Magnetic Field

The spectrum of both non-relativistic and relativistic fermions in a magnetic field has long attracted attention as a theoretical problem since the discovery of Landau levels. More recently, electronic properties of two-dimensional electron gas systems in a strong magnetic field became of experimental interest due to the discovery of the integer and fractional quantum Hall effects [81, 82]. Quantum Hall physics has also been seen for Dirac fermions in graphene [83]. This motivates us to study birefringent fermions coupled to a magnetic field. In this chapter, we obtain the generalization of Landau levels for birefringent fermions and their wavefunctions in the Landau gauge and discuss their consequences for the Integer Quantum Hall effect.

5.1 Birefringent Fermions in a Magnetic Field

Whilst we originally derived birefringent fermions in a tight binding model with an artificial magnetic field, we are free to ask what the spectrum of birefringent fermions looks like when a magnetic field is present, without asking about specific tight-binding models that might be required to realize them. Hence, we now derive the Landau level energy spectrum by coupling a magnetic field to the effective Hamiltonian. We recall that in zero field

$$H_k = 2J_0 \left[\left(\gamma^0\gamma^1 + i\beta\gamma^3 \right) k_x + \left(\gamma^0\gamma^2 + i\beta\gamma^5 \right) k_y \right]. \tag{5.1}$$

To include a magnetic field, we transform to real space and make the the minimal coupling assumption $\vec{k} \to \vec{k} + \vec{A}$ (we have set $\hbar = 1$ and the charge to unity). We use the Landau gauge $\vec{A} = (0, xB, 0)$. We will seek the Landau levels by solving the eigenvalue problem $(E - H)\Psi = 0$.

Noting that the system is translationally invariant in the y-direction, we make the following ansatz for the eigenstates:

$$\psi(x,y) = e^{ik_y y} \begin{pmatrix} f_1 \\ f_2 \\ f_3 \\ f_4 \end{pmatrix}.$$

We also make the change of variables $\xi = \dfrac{k_y + Bx}{\sqrt{B}}$, which implies $\dfrac{\partial}{\partial x} = \sqrt{B}\dfrac{\partial}{\partial \xi}$. Rescaling the energy to $\varepsilon = E/2J_0\sqrt{B}$, we obtain the eigenvalue equation

$$\begin{pmatrix} \varepsilon & -(1+\beta)\xi & i(1+\beta)\dfrac{\partial}{\partial\xi} & 0 \\ (1+\beta)\xi & -\varepsilon & 0 & i(1-\beta)\dfrac{\partial}{\partial\xi} \\ -i(1+\beta)\dfrac{\partial}{\partial\xi} & 0 & -\varepsilon & (1-\beta)\xi \\ 0 & i(\beta-1)\dfrac{\partial}{\partial\xi} & (\beta-1)\xi & \varepsilon \end{pmatrix} \begin{pmatrix} f_1 \\ f_2 \\ f_3 \\ f_4 \end{pmatrix} = 0. \tag{5.2}$$

By treating this as a system of four simultaneous equations and through judicious combination of the four equations we may obtain the following differential equation for f_1:

$$\left[\varepsilon^2 - (1-\beta)^2\xi^2 + (1-\beta)^2 \frac{\partial^2}{\partial\xi^2} \right] \left[\varepsilon^2 - (1+\beta)^2\xi^2 + (1+\beta)^2 \frac{\partial^2}{\partial\xi^2} \right] f_1 - (1-\beta^2)^2 f_1 = 0.$$

To solve this equation, we try a solution of the form $f_1 = H_n(\xi)\exp\left(-\dfrac{1}{2}\xi^2\right)$, where $H_n(\xi)$ is the n^{th} Hermite polynomial (we will not bother with normalization constants) and we arrive at the following equation for the energy

$$\varepsilon^4 - 2(2n+1)(1+\beta^2)\varepsilon^2 + 4n(n+1)(1-\beta^2)^2 = 0.$$

It is straightforward to solve this equation to find the generalization of Landau levels for birefringent fermions, which depends on the integers n and the parameter β.

$$\varepsilon_{n,\beta} = \pm\sqrt{(2n+1)(1+\beta^2) \pm \sqrt{(2n+1)^2(1+\beta^2)^2 - 4n(n+1)(1-\beta^2)^2}}.$$

To connect to standard Landau levels, first consider $\beta = 0$. Doing so, we arrive at $\varepsilon = \pm\sqrt{2n+2}$, and $\varepsilon = \pm\sqrt{2n}$, as we would expect, in contrast to non-relativistic Landau levels with energies $\varepsilon_n = (n+1/2)$ (in the same units). In Fig. 5.1, we show the energy levels as a function of β for $n = 0,1,2,3,4,5$. Note that in the limit $\beta \to 1$, half of the levels go to $\varepsilon = 0$ (the flat band found at $\varepsilon = 0$ when $B = 0$) and the other half go to $\varepsilon = \pm\sqrt{2(2n+1)}$.

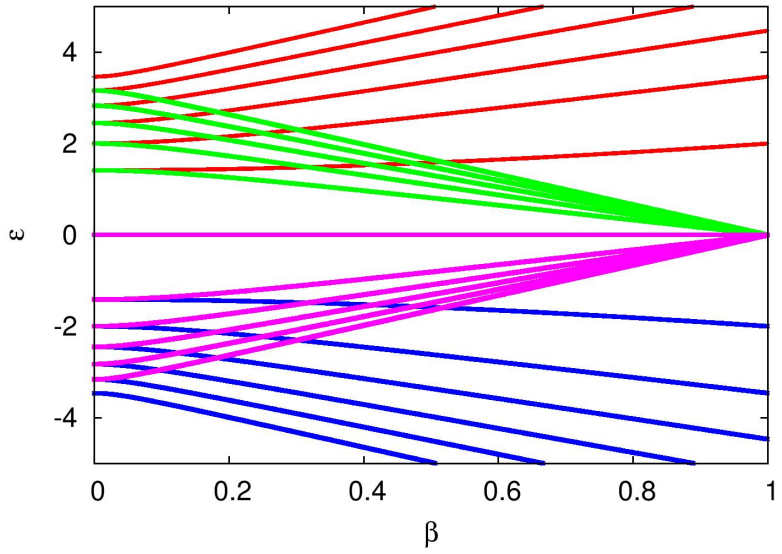

Figure 5.1: Energy spectrum (ε_n, β) as a function of β for $n = 0,1,2,3,4,5$.

Having found f_1, we can then find f_4 from

$$f_4 = \left(\frac{i}{1-\beta^2}\right)\left[\varepsilon^2 - (1+\beta)^2\xi^2 + (1+\beta)^2\frac{\partial^2}{\partial\xi^2}\right] f_1.$$

Taking $f_1 = H_n(\xi)\exp\left(-\frac{1}{2}\xi^2\right)$, f_4 can be determined as:

$$f_4 = \left(\frac{i}{1-\beta^2}\right)\left[\varepsilon^2 - (1+\beta)^2(1+2n)\right]H_n(\xi)\exp\left(-\frac{1}{2}\xi^2\right).$$

when β is non zero, noting that we can write $\varepsilon_{n,\beta} = \pm\sqrt{f_n \pm \sqrt{f_n^2 - g_n}}$,
with $f_n = (2n+1)(1+\beta^2)$ and $g_n = 4n(n+1)(1-\beta^2)^2$, we get the general form of f_4 as follows:

$$f_4 = \left(\frac{i}{1-\beta^2}\right)\left[\pm\sqrt{f_n^2 - g_n} - 2\beta(2n+1)\right]H_n(\xi)\exp\left(-\frac{1}{2}\xi^2\right),$$

with the $\pm$ depending on the particular energy eigenvalue. We can obtain f_2 from f_1 and f_4 through

$$\varepsilon f_2 = (1+\beta)\xi f_1 + i(1-\beta)\frac{\partial}{\partial\xi}f_4,$$

and f_3 may also be obtained from f_1 and f_4 using

$$\varepsilon f_3 = -i(1+\beta)\frac{\partial}{\partial\xi}f_1 + (1-\beta)\xi f_4.$$

Following through the solutions for f_2, f_3, f_4 for each of the energy eigenvalues, we find the following eigenfunctions, which are summarized below.
For $n \neq 0$ and $\varepsilon \neq 0$ and eigenvalue

$$\varepsilon_{n,++} = \sqrt{(2n+1)(1+\beta^2) + \sqrt{(2n+1)^2(1+\beta^2)^2 - 4n(n+1)(1-\beta^2)^2}},$$

the eigenfunction is

$$
\begin{aligned}
f_1 &= H_n(\xi)e^{-\frac{1}{2}\xi^2}, \\
f_2 &= \left(\frac{1}{(1+\beta)\varepsilon_{n,++}}\right)\left\{\left[(1+\beta)^2+2\beta(2n+1)-\sqrt{f_n^2-g_n}\right]\xi H_n(\xi)\right. \\
&\quad \left.-\left(2\beta(2n+1)-\sqrt{f_n^2-g_n}\right)H_{n+1}(\xi)\right\}e^{-\frac{1}{2}\xi^2}, \\
f_3 &= \left(\frac{-i}{(1+\beta)\varepsilon_{n,++}}\right)\left\{\left[(1+\beta)^2-2\beta(2n+1)-\sqrt{f_n^2-g_n}\right]\xi H_n(\xi)-(1+\beta)^2H_{n+1}(\xi)\right\}e^{-\frac{1}{2}\xi^2}, \\
f_4 &= \left(\frac{i}{1-\beta^2}\right)\left[\sqrt{f_n^2-g_n}-2\beta(2n+1)\right]H_n(\xi)e^{-\frac{1}{2}\xi^2}.
\end{aligned}
$$

For the energy eigenvalue:

$$\varepsilon_{n,-+} = -\sqrt{f_n+\sqrt{f_n^2-g_n}},$$

$$
\begin{aligned}
f_1 &= H_n(\xi)e^{-\frac{1}{2}\xi^2}, \\
f_2 &= \left(\frac{1}{(1+\beta)\varepsilon_{n,-+}}\right)\left\{\left[(1+\beta)^2+2\beta(2n+1)-\sqrt{f_n^2-g_n}\right]\xi H_n(\xi)\right. \\
&\quad \left.-\left(2\beta(2n+1)-\sqrt{f_n^2-g_n}\right)H_{n+1}(\xi)\right\}e^{-\frac{1}{2}\xi^2}, \\
f_3 &= \left(\frac{-i}{(1+\beta)\varepsilon_{n,-+}}\right)\left\{\left[(1+\beta)^2-2\beta(2n+1)-\sqrt{f_n^2-g_n}\right]\xi H_n(\xi)-(1+\beta)^2H_{n+1}(\xi)\right\}e^{-\frac{1}{2}\xi^2}, \\
f_4 &= \left(\frac{i}{1-\beta^2}\right)\left[\sqrt{f_n^2-g_n}-2\beta(2n+1)\right]H_n(\xi)e^{-\frac{1}{2}\xi^2}.
\end{aligned}
$$

For the case of the energy dispersion

$$\varepsilon_{n,+-} = \sqrt{f_n-\sqrt{f_n^2-g_n}},$$

$$
\begin{aligned}
f_1 &= H_n(\xi)e^{-\frac{1}{2}\xi^2}, \\
f_2 &= \left(\frac{1}{(1+\beta)\varepsilon_{n,+-}}\right)\left\{\left[(1+\beta)^2+2\beta(2n+1)+\sqrt{f_n^2-g_n}\right]\xi H_n(\xi)\right. \\
&\quad \left.-\left(2\beta(2n+1)+\sqrt{f_n^2-g_n}\right)H_{n+1}(\xi)\right\}e^{-\frac{1}{2}\xi^2}, \\
f_3 &= \left(\frac{-i}{(1+\beta)\varepsilon_{n,+-}}\right)\left\{\left[(1+\beta)^2-2\beta(2n+1)+\sqrt{f_n^2-g_n}\right]\xi H_n(\xi)-(1+\beta)^2H_{n+1}(\xi)\right\}e^{-\frac{1}{2}\xi^2}, \\
f_4 &= \left(\frac{-i}{1-\beta^2}\right)\left[\sqrt{f_n^2-g_n}+2\beta(2n+1)\right]H_n(\xi)e^{-\frac{1}{2}\xi^2}.
\end{aligned}
$$

Finally, for energy dispersion

$$\varepsilon_{n,--} = -\sqrt{f_n-\sqrt{f_n^2-g_n}},$$

we have

$$
\begin{aligned}
f_1 &= H_n(\xi)e^{-\frac{1}{2}\xi^2}, \\
f_2 &= \left(\frac{1}{(1+\beta)\varepsilon_{n,--}}\right)\left\{\left[(1+\beta)^2+2\beta(2n+1)+\sqrt{f_n^2-g_n}\right]\xi H_n(\xi)\right. \\
&\quad \left.-\left(2\beta(2n+1)+\sqrt{f_n^2-g_n}\right)H_{n+1}(\xi)\right\}e^{-\frac{1}{2}\xi^2}, \\
f_3 &= \left(\frac{-i}{(1+\beta)\varepsilon_{n,--}}\right)\left\{\left[(1+\beta)^2-2\beta(2n+1)+\sqrt{f_n^2-g_n}\right]\xi H_n(\xi)-(1+\beta)^2H_{n+1}(\xi)\right\}e^{-\frac{1}{2}\xi^2}, \\
f_4 &= \left(\frac{-i}{1-\beta^2}\right)\left[\sqrt{f_n^2-g_n}+2\beta(2n+1)\right]H_n(\xi)e^{-\frac{1}{2}\xi^2}.
\end{aligned}
$$

For $n=0$, the energy is either $\varepsilon=0$ or $\varepsilon=\pm\sqrt{2(1+\beta^2)}$. In the expressions above, for f_2 and f_3, we divided by ε. This is clearly inappropriate when $\varepsilon=0$. Hence we consider

the case $n = 0$ separately. When the energy dispersion is $\varepsilon = \varepsilon_{0,++} = \sqrt{2(1+\beta^2)}$, then the set of eigenfunctions are:

$$\begin{aligned} f_1 &= e^{-\frac{1}{2}\xi^2}, \\ f_2 &= \left(\frac{1}{(1+\beta)\varepsilon_{0,++}}\right)\{4\beta\xi + (1-\beta)^2 2\xi\}\, e^{-\frac{1}{2}\xi^2}, \\ f_3 &= \left(\frac{i}{\varepsilon_{0,++}}\right)(1+\beta)2\xi e^{-\frac{1}{2}\xi^2}, \\ f_4 &= \left(\frac{i}{1+\beta}\right)(1-\beta)e^{-\frac{1}{2}\xi^2}. \end{aligned}$$

where we noted $H_0(\xi) = 1$ and $H_1(\xi) = 2\xi$. Also for the energy dispersion:

$$\varepsilon_{0,-+} = -\sqrt{2(1+\beta^2)},$$

$$\begin{aligned} f_1 &= e^{-\frac{1}{2}\xi^2}, \\ f_2 &= \left(\frac{1}{(1+\beta)\varepsilon_{0,-+}}\right)\left\{4\beta\xi + (1-\beta)^2 2\xi\right\} e^{-\frac{1}{2}\xi^2}, \\ f_3 &= \left(\frac{i}{\varepsilon_{0,-+}}\right)(1+\beta)2\xi e^{-\frac{1}{2}\xi^2}, \\ f_4 &= \left(\frac{i}{1+\beta}\right)(1-\beta)e^{-\frac{1}{2}\xi^2}. \end{aligned}$$

For the case of the energy dispersion $\varepsilon_{0,+-} = \varepsilon_{0,--} = 0$, one eigenfunction is

$$\begin{aligned} f_1 &= e^{-\frac{1}{2}\xi^2}, \\ f_4 &= -i\left(\frac{1+\beta}{1-\beta}\right)e^{-\frac{1}{2}\xi^2}. \end{aligned}$$

Now, when $\varepsilon = 0$, f_2 and f_3 decouple from f_1 and f_4 in Eq. (5.2), in which case we either have a solution with $f_1, f_4 \neq 0$, $f_2 = f_3 = 0$ or vice versa, in which case we obtain $f_3 = if_2 = ie^{-\xi^2/2}$.

5.2 Integer Quantum Hall Effect in Birefringent Fermions

The integer quantum Hall effect in graphene shows plateaux at $\sigma = \pm(4n+2)e^2/h$, which is a result of the four fold degeneracy (two from spin and two from valley degrees of freedom) for the $n \neq 0$ Landau levels and two fold degeneracy for the $n = 0$ Landau level. In our model, when $\beta = 0$, one would expect to see an integer quantum Hall effect with conductivities $\sigma = fe^2/\hbar$ with $f = \pm(2n+1)$, since for spinless fermions, the system lacks spin degeneracy, but there is still a two-fold degeneracy for $n \neq 0$ associated with the doubly degenerate Dirac cones. When $\beta \neq 0$, the breaking of degeneracy of the Dirac cones implies that the integer quantum Hall effect will also be modified so that conductivities for all non-zero integers should be present, i.e. $\sigma = fe^2/\hbar$ with $f = \pm(n+1)$.

5.3 Summary

In this chapter, we studied birefringent fermions coupled to a magnetic field and obtained the generalization of Landau levels for birefringent fermions. We also discussed consequences of fermion birefringence for the integer quantum Hall effect and the fact that fermion birefringence allows for more quantum Hall states than regular Dirac fermions.

Chapter 6

Conclusions and Future Directions

In this thesis, birefringent fermions have been introduced as the low energy excitations in a particular tight binding model that emerged from a scheme to realize an artificial magnetic field for cold atoms in an optical lattice. In Chapter 3, we developed the theory of non-interacting birefringent fermions. In particular, the low energy theory was discussed and the appropriate Dirac-like Hamiltonian was analyzed.

We showed that the model displays the unusual property that chiral symmetry is broken in the kinetic energy rather than via mass terms. Moreover, we show that this has the consequence that the doubly degenerate Dirac cones split into two cones with two separate slopes, analogous to a situation in which there are two speeds of light for fermionic excitations, similar to birefringence of light in crystals such as calcite. In Chapter 4, we considered both nearest neighbour and next-nearest neighbour interactions at the mean field level. We showed phase diagrams as a function of birefringence parameter β, and found that in the presence of both nearest neighbour and next nearest neighbour interactions, fermion birefringence can stabilize a circulating current phase that is not favoured for regular Dirac fermions. Finally, we considered the effect of a magnetic field on birefringent fermion and its implications for the integer quantum Hall effect.

6.1 Future Directions

There are a number of future directions that could be pursued from the work in this thesis. One generalization would be to consider fermions with spin and to study the effects of

on-site Hubbard interactions, which could require an approach similar to those used to study QED_3 in high temperature superconductors [84]. Another might be to consider the combined effect of a magnetic field and interactions and possible phases that might arise in such a case. One might also wonder if we can generalize birefringent fermions to higher dimensions than two? To answer that question, we consider a tight binding model for spinless fermions on a cubic lattice in three dimensions, similar to that discussed by Hosur *et al.* [85]. The unit cell is illustrated in Fig. 6.1. There is π-flux through each of the faces of the cube and two sides with hopping amplitude J_- and two with J_+ for each plaquette of the cube too. With the labelling in Fig. 6.1, one can define an 8-component fermion with

$$f^\dagger = (C_1^\dagger, C_2^\dagger, C_3^\dagger, C_4^\dagger, C_5^\dagger, C_6^\dagger, C_7^\dagger, C_8^\dagger),$$

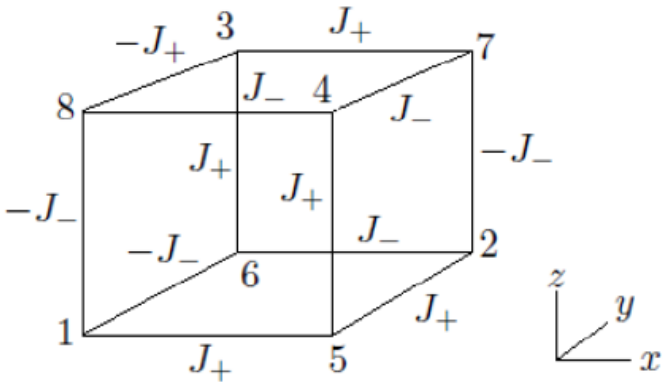

Figure 6.1: Unit cell of a three-dimensional tight-binding model with birefringent fermionic excitations.

and the tight binding Hamiltonian may be written as

$$H = \sum_k f_k^\dagger H_k f_k.$$

The non-zero elements of hopping matrix, H_k, are
$H_{15} = J_+ \cos k_x$, $H_{16} = -J_- \cos k_y$, $H_{18} = -J_- \cos k_z$, $H_{25} = J_+ \cos k_y$, $H_{26} = J_- \cos k_x$, $H_{27} = -J_- \cos k_z$, $H_{36} = J_+ \cos k_z$, $H_{37} = J_+ \cos k_x$, $H_{38} = -J_+ \cos k_y$, $H_{45} = J_+ \cos k_z$, $H_{47} = J_- \cos k_y$, and $H_{48} = J_- \cos k_x$.

This may be written in terms of the Pauli matrices in the following form:

$$\begin{aligned} H_k &= J\cos k_x(\sigma_1\otimes I_2\otimes I_2)+J\beta\cos k_x(\sigma_1\otimes I_2\otimes\sigma_3)+J\cos k_y(\sigma_2\otimes I_2\otimes\sigma_2) \\ &\quad +J\beta\cos k_y(\sigma_1\otimes\sigma_3\otimes\sigma_1)+J\cos k_z(\sigma_2\otimes\sigma_2\otimes\sigma_1)+J\beta\cos k_z(\sigma_1\otimes\sigma_1\otimes\sigma_1). \end{aligned}$$

To find the spectrum, we square the Hamiltonian, which yields

$$H_k^2 = \begin{pmatrix} M_k^+ & 0 \\ 0 & M_k^- \end{pmatrix},$$

where

$$\begin{aligned} M_k^+ &= \varepsilon_0 I_4+\varepsilon_1(I_2\otimes\sigma_3)-\varepsilon_2(\sigma_3\otimes\sigma_3)-\varepsilon_3(\sigma_3\otimes I_2)+\alpha_1(\sigma_3\otimes\sigma_1+I_2\otimes\sigma_1) \\ &\quad +\alpha_2(\sigma_1\otimes\sigma_1-\sigma_2\otimes\sigma_2)+\alpha_3(\sigma_1\otimes I_2-\sigma_1\otimes\sigma_3), \end{aligned}$$

and

$$\begin{aligned} M_k^- &= \varepsilon_0 I_4+\varepsilon_1(I_2\otimes\sigma_3)+\varepsilon_2(\sigma_3\otimes\sigma_3)+\varepsilon_3(\sigma_3\otimes I_2)+\alpha_1(\sigma_3\otimes\sigma_1-I_2\otimes\sigma_1) \\ &\quad +\alpha_2(\sigma_1\otimes\sigma_1+\sigma_2\otimes\sigma_2)+\alpha_3(\sigma_1\otimes\sigma_3-\sigma_1\otimes I_2), \end{aligned}$$

with
$\varepsilon_0 = J^2(1+\beta^2)[\cos^2 k_x+\cos^2 k_y+\cos^2 k_z]$,
$\varepsilon_1 = 2\beta J^2\cos^2 k_x$, $\varepsilon_2 = 2\beta J^2\cos^2 k_y$,
$\varepsilon_3 = 2\beta J^2\cos^2 k_z$, $\alpha_1 = 2\beta J^2\cos k_x\cos k_y$,
$\alpha_2 = 2\beta J^2\cos k_x\cos k_z$, $\alpha_3 = 2\beta J^2\cos k_y\cos k_z$.

We can diagonalize the 4×4 matrices M_k^+ and M_k^- separately and find that the eigenvalues of H_k are $E_k = \pm J(1\pm\beta)\sqrt{\cos^2 k_x+\cos^2 k_y+\cos^2 k_z}$ each with 2-fold degeneracy implying a low energy spectrum around the 8 Dirac points $\vec{K} = (\pm\pi/2,\pm\pi/2,\pm\pi/2)$ of $\varepsilon_{\vec{q}} = \pm J_\pm|\vec{q}|$, with $\vec{q} = \vec{k}-\vec{K}$. Future work on this model could involve studying possible ordered phases from interactions and their dependence on the birefringence parameter.

Appendix A

Terms neglected in the derivation of the tight-binding model

In deriving the effective Hamiltonian, Eq. (2.3), we kept only the lowest order terms in $J\tau/\hbar$. The relevant next order terms are:

$$\frac{1}{2}\left[\frac{i\tau J}{\hbar}\sum_{x_1,y_1}\left\{e^{2\pi i\alpha y_1}c^{\dagger}_{x_{1+1},y_1}c_{x_1,y_1}+\beta e^{2\pi i\alpha x_1}c^{\dagger}_{x_1,y_{1+1}}c_{x_1,y_1}+\text{H.c}\right\},\right.$$
$$\left.+\frac{i\tau}{2\hbar}J\sum_{x_2,y_2}\left\{c^{\dagger}_{x_{2+1},y_2}c_{x_2,y_2}+c^{\dagger}_{x_2,y_{2+1}}c_{x_2,y_2}+\text{H.c}\right\}\right],$$

which can be evaluated to be:

$$
\begin{aligned}
&-\frac{\tau^2 J^2}{4\hbar^2}\sum_{x_1,y_1}\sum_{x_2,y_2}\Big\{ e^{2\pi i\alpha y_1}[c^\dagger_{x_{1+1},y_1}c_{x_1,y_1},c^\dagger_{x_{2+1},y_2}c_{x_2,y_2}]+e^{2\pi i\alpha y_1}[c^\dagger_{x_{1+1},y_1}c_{x_1,y_1},c^\dagger_{x_2,y_{2+1}}c_{x_2,y_2}]\\
&+e^{2\pi i\alpha y_1}[c^\dagger_{x_{1+1},y_1}c_{x_1,y_1},c^\dagger_{x_2,y_2}c_{x_{2+1},y_2}]+e^{2\pi i\alpha y_1}[c^\dagger_{x_{1+1},y_1}c_{x_1,y_1},c^\dagger_{x_2,y_2}c_{x_2,y_{2+1}}]\\
&+e^{-2\pi i\alpha y_1}[c^\dagger_{x_1,y_1}c_{x_{1+1},y_1},c^\dagger_{x_{2+1},y_2}c_{x_2,y_2}]+e^{-2\pi i\alpha y_1}[c^\dagger_{x_1,y_1}c_{x_1+1,y_1},c^\dagger_{x_2,y_2+1}c_{x_2,y_2}]\\
&+e^{-2\pi i\alpha y_1}[c^\dagger_{x_1,y_1}c_{x_1+1,y_1},c^\dagger_{x_2,y_2}c_{x_2+1,y_2}]+e^{-2\pi i\alpha y_1}[c^\dagger_{x_1,y_1}c_{x_1+1,y_1},c^\dagger_{x_2,y_2}c_{x_2,y_2+1}]\\
&+\beta e^{2\pi i\alpha x_1}[c^\dagger_{x_1,y_1+1}c_{x_1,y_1},c^\dagger_{x_2+1,y_2}c_{x_2,y_2}]+\beta e^{2\pi i\alpha x_1}[c^\dagger_{x_1,y_1+1}c_{x_1,y_1},c^\dagger_{x_2,y_2}c_{x_2+1,y_2}]\\
&+\beta e^{2\pi i\alpha x_1}[c^\dagger_{x_1,y_1+1}c_{x_1,y_1},c^\dagger_{x_2,y_2}c_{x_2,y_2+1}]+\beta e^{2\pi i\alpha x_1}[c^\dagger_{x_1,y_1+1}c_{x_1,y_1},c^\dagger_{x_2,y_{2+1}}c_{x_2,y_2}]\\
&+\beta e^{-2\pi i\alpha x_1}[c^\dagger_{x_1,y_1}c_{x_1,y_1+1},c^\dagger_{x_2+1,y_2}c_{x_2,y_2}]+\beta e^{-2\pi i\alpha x_1}[c^\dagger_{x_1,y_1}c_{x_1,y_1+1},c^\dagger_{x_2,y_2+1}c_{x_2,y_2}]\\
&+\beta e^{-2\pi i\alpha x_1}[c^\dagger_{x_1,y_1}c_{x_1,y_1+1},c^\dagger_{x_2,y_2}c_{x_2+1,y_2}]+\beta e^{-2\pi i\alpha x_1}[c^\dagger_{x_1,y_1}c_{x_1,y_1+1},c^\dagger_{x_2,y_2}c_{x_2,y_2+1}]\Big\}.
\end{aligned}
$$

Now, $\{c_a,c_b^\dagger\}=\delta_{ab}$, and so we have:

$$
\begin{aligned}
&\left[c^\dagger_{x_a,y_a}c_{x_b,y_b},c^\dagger_{x_c,y_c}c_{x_d,y_d}\right]\\
=\;& c^\dagger_{x_a,y_a}c_{x_b,y_b}c^\dagger_{x_c,y_c}c_{x_d,y_d}-c^\dagger_{x_c,y_c}c_{x_d,y_d}c^\dagger_{x_a,y_a}c_{x_b,y_b}\\
=\;& c^\dagger_{x_a,y_a}\{\delta_{x_b,x_c}\delta_{y_b,y_c}-c^\dagger_{x_c,y_c}c_{x_b,y_b}\}c_{x_d,y_d}-c^\dagger_{x_c,y_c}\{\delta_{x_a,x_a}\delta_{y_a,y_d}-c_{x_a,y_a}c^\dagger_{x_d,y_d}\}c_{x_b,y_b}\\
=\;& \delta_{x_b,x_c}\delta_{y_b,y_c}c_{x_a,y_a}c^\dagger_{x_d,y_d}-\delta_{x_a,x_d}\delta_{y_a,y_d}c_{x_c,y_c}c^\dagger_{x_b,y_b}
\end{aligned}
$$

Therefore, the additional terms are

$$
\begin{aligned}
&-\frac{\tau^2 J^2}{4\hbar^2}\sum_{x_1,y_1}\Bigg\{ e^{2\pi i\alpha y_1}\Big[c_{x_1+1,y_1}c^\dagger_{x_1-1,y_1} - c_{x_1+2,y_1}c^\dagger_{x_1,y_1} + c_{x_1+1,y_1}c^\dagger_{x_1,y_1-1} - c_{x_1+1,y_1+1}c^\dagger_{x_1,y_1} \\
&+ c_{x_1+1,y_1}c^\dagger_{x_1+1,y_1} - c_{x_1,y_1}c^\dagger_{x_1,y_1} + c_{x_1+1,y_1}c^\dagger_{x_1,y_1+1} - c_{x_1+1,y_1-1}c^\dagger_{x_1,y_1}\Big] \\
&+ e^{-2\pi i\alpha y_1}\Big[c_{x_1,y_1}c^\dagger_{x_1,y_1} - c_{x_1+1,y_1}c^\dagger_{x_1+1,y_1} + c_{x_1,y_1}c^\dagger_{x_1+1,y_1-1} - c_{x_1,y_1+1}c^\dagger_{x_1+1,y_1} \\
&+ c_{x_1,y_1}c^\dagger_{x_1+2,y_1} - c_{x_1-1,y_1}c^\dagger_{x_1+1,y_1} + c_{x_1,y_1}c^\dagger_{x_1+1,y_1+1} - c_{x_1,y_1-1}c^\dagger_{x_1+1,y_1}\Big] \\
&+ \beta e^{2\pi i\alpha x_1}\Big[c_{x_1,y_1+1}c^\dagger_{x_1-1,y_1} - c_{x_1,y_1}c^\dagger_{x_1,y_1} + c_{x_1,y_1+1}c^\dagger_{x_1+1,y_1} - c_{x_1-1,y_1+1}c^\dagger_{x_1,y_1} \\
&+ c_{x_1,y_1}c^\dagger_{x_1,y_1+1} - c_{x_1,y_1}c^\dagger_{x_1,y_1} + c_{x_1,y_1}c^\dagger_{x_1,y_1-1} - c_{x_1,y_1+2}c^\dagger_{x_1,y_1}\Big] \\
&+ \beta e^{-2\pi i\alpha x_1}\Big[c_{x_1,y_1}c^\dagger_{x_1-1,y_1+1} - c_{x_1+1,y_1}c^\dagger_{x_1,y_1+1} + c_{x_1,y_1}c^\dagger_{x_1,y_1} - c_{x_1,y_1+1}c^\dagger_{x_1,y_1+1} \\
&+ c_{x_1,y_1}c^\dagger_{x_1,y_1} - c_{x_1-1,y_1}c^\dagger_{x_1,y_1+1} + c_{x_1,y_1}c^\dagger_{x_1,y_1+2} - c_{x_1,y_1-1}c^\dagger_{x_1,y_1+1}\Big]\Bigg\}.
\end{aligned}
$$

We have not investigated all of these terms, but note that at least those which correspond to next nearest neighbour hopping from sites A to D or B to C will preserve the birefringent property of the spectrum.

Bibliography

[1] S. N. Bose, Z. Phys. **26**, 178 (1924).

[2] A. Einstein, Sitzungsber. Kgl. Preuss. Akad. Wiss., 261-267 (1924).

[3] M. H. Anderson, J. R. Ensher, M. R. Matthews, C. E. Wieman, and E. A. Cornell, Science **269**, 198 (1995).

[4] B. DeMarco, and D. Jin, Science **285**, 1703 (1999).

[5] F. Schreck, L. Khaykovich, K. L. Corwin, G. Ferrari, T. Bourdel, J. Cubizolles, and C. Salomon Phys. Rev. Lett. **87**, 080403 (2001).

[6] A. K. Truscott, K. E. Strecker, W. I. McAlexander, G. B. Partridge, and R. G. Hulet. Science **291**, 2570 (2001).

[7] P. S. Jessen and I. H. Deutsch, Adv. Atom. Mol. Opt. Phy **37**, 95 (1996).

[8] D. R. Meacher, Contemp. Phys. **39**, 329 (1998).

[9] G. Grynberg and C. Robilliard, Phys. Rep. **355**, 335 (2001).

[10] O. Morsch and M. Oberthaler, Rev. Mod. Phys. **78**, 179 (2006).

[11] K. S. Novoselov, A. K. Geim, S. V. Morozov, D. Jiang, Y. Zhang, S. V. Dubonos, I. V. Crigorieva, and A. A. Firsov, Science **306**, 666 (2004).

[12] R. P. Feynman, Opt. News **11**, 11 (1985).

[13] R. P. Feynman, Found. Phys. **16**, 507 (1986).

[14] I. Bloch, Phys. World **17**, 25 (2004).

[15] I. Bloch, Nature **453**, 1016 (2008).

[16] G. Raithel, G. Birkl, A. Kastberg, W. D. Phillips, and S. L. Rolston, Phys. Rev. Lett. **78**, 630 (1997).

[17] I. Bloch, J. Dalibard and W. Zwerger, Rev. Mod. Phys. **80**, 885 (2008).

[18] S. Friebel, C. D'Andrea, J. Walz, M. Weitz, and T. W. Hänsch, Phys. Rev. A **57**, R20 (1998).

[19] M. Raizen, C. Salomon, and Q. Niu, Phys. Today **50**, 30 (1997).

[20] R. V. Chamberlin, M. J. Naughton, X. Yan, L. Y. Chiang, S. Y. Hsu, Phys. Rev. Lett. **60**, 1189 (1988).

[21] A. S. Sørensen, E. Demler, and M. D. Lukin, Phys. Rev. Lett. **94**, 086803 (2005).

[22] D. Jaksch and P. Zoller, New J. Phys. **5**, 56 (2003).

[23] N. R. Cooper, Adv. Phys. **57**, 539 (2008).

[24] N. R. Cooper and N. K. Wilkin, Phys. Rev. B **60**, 16279 (1999).

[25] A. Klein and D. Jaksch, Europhys. Lett. **85**, 13001 (2009).

[26] M. Rosenkranz, A. Klein, and D. Jaksch, Phys. Rev. A **81**, 013607 (2010).

[27] F. Gerbier and J. Dalibard, New J. Phys. **12**, 033007 (2010).

[28] T.-L. Ho and S. Zhang, arXiv:1007.0650v1.

[29] D. Makogon, I. B. Spielman, and C. Morais Smith, Europhys Lett. **97**, 33002 (2012).

[30] A. H. Castro Neto, F. Guinea, N. M. R. Peres, K. S. Novoselov, and A. K. Geim, Rev. Mod. Phys. **81**, 109 (2009).

[31] L.-K. Lim, A. Hemmerich, and C. Morais Smith, Phys. Rev. A **81**, 023404 (2010).

[32] L. Tarruell, D. Greif, T. Uehlinger, G. Jotzu and T. Esslinger, Nature **483**, 302 (2012).

[33] V. Schweikhard, I. Coddington, P. Engels, V. P. Mogendorff, and E. A. Cornell, Phys. Rev. Lett. **92**, 040404 (2004).

[34] K. K. Gomes, W. Mar, W. Ko, F. Guinea, and H. C. Manoharan, Nature **483**, 306 (2012).

[35] J. Simon and M. Greiner, Nature **483**, 282 (2012).

[36] Y.-J. Lin, R. L. Compton, K. Jiménez-García, J. V. Porto and I. B. Spielman, Nature **462**, 628 (2009).

[37] K. W. Madison, F. Chevy, W. Wohlleben, and J. Dalibard, Phys. Rev. Lett. **84**, 806 (2000).

[38] M. Aidelsburger, M. Atala, S. Nascimbene, S. Trotzky, Y.-A. Chen, and I. Bloch, Phys. Rev. Lett. **107**, 255301 (2011).

[39] R. Peierls, Z. Phys. **80**, 763 (1933). 1).

[40] S. Tung, V. Schweikhard, and E. A. Cornell, Phys. Rev. Lett. **97**, 240402 (2006).

[41] R. A. Williams, S. Al-Assam, and C. J. Foot, Phys. Rev. Lett. **104**, 050404 (2010).

[42] E. A. Cornell and C. E. Wieman, Rev. Mod. Phys. **74**, 875 (2002).

[43] W. Ketterle, Rev. Mod. Phys. **74**, 1131 (2002).

[44] E. Hodby, G. Hechenblaikner, S. A. Hopkins, O. M. Marago, and C. J. Foot, Phys. Rev. Lett. **88**, 010405 (2002).

[45] J. R. Abo-Shaeer, C. Raman, J. M. Vogels, and W. Ketterle, Science **292**, 476 (2001).

[46] G. Juzeliunas, Physics **2**, 25 (2009).

[47] N. R. Cooper, Phys. Rev. Lett. **106**, 175301 (2011).

[48] P. J. Zomer, S. P. Dash, N. Tombros, and B. J. van Wees. App. Phys. Lett. **99**, 232104 (2011).

[49] Y. Wu, Y.-M. Lin, A. A. Bol, K. A. Jenkins, F. Xia, D. B. Farmer, Y. Zhu, and P. Avouris, Nature **472**, 74, (2011).

[50] R. R. Nair, P. Blake, A. N. Grigorenko, K. S. Novoselov, T. J. Booth, T. Stauber, N. M. R. Peres, and A. K. Geim. Science **320**, 1308 (2008).

[51] X. Wang, L. Zhi, and K. Mullen. Nano Letters **8**, 323 (2008).

[52] J. Wu, M. Agrawal, H. A. Becerril, Z. Bao, Z. Liu, Y. Chen, and P. Peumans. Am. Chem. Soc. Nano **4**, 43 (2010).

[53] Y. Zhu, Z. Sun, Z. Yan, Z. Jin, and J. M. Tour, Am. Chem. Soc. Nano **5**, 6472 (2011).

[54] K. S. Novoselov, V. I. Falko, L. Colombo, P. R. Gellert, M. G. Schwab and K. Kim, Nature **490**, 192 (2012).

[55] Z. Lan, N. Goldman, A. Bermudez, W. Lu, and P. Ohberg, Phys. Rev. B **84**, 165115 (2011).

[56] Z. Lan, A. Celi, W. Lu, P. Ohberg, and M. Lewenstein, Phys. Rev. Lett. **107**, 253001 (2011).

[57] M. P. Kennett, N. Komeilizadeh, K. Kaveh, and P. M. Smith, Phys. Rev. A **83**, 053636 (2011).

[58] D. R. Hofstadter, Phys. Rev. B **14**, 2239 (1976).

[59] A. Barelli, J. Bellissard, and R. Rammal, J. Phys. France **51**, 2167 (1990).

[60] M. C. Chang and Q. Niu, Phys. Rev. B **50**, 10843 (1994).

[61] G.-Y. Oh, Phys. Rev. B **60**, 1939 (1999).

[62] M. Ando, I. Suguru, K. Shingo and I. Yasuhiro, J. Phys. Soc. Jpn. **68**, 3462 (1999).

[63] M.-C. Chang and M.-F. Yang, Phys. Rev. B **69**, 115108 (2004).

[64] Y. Iye, E. Kuramochi, M. Hara, A. Endo and S. Katsumoto Phys. Rev. B **70**, 144524 (2004).

[65] Y.-F. Wang and C.-D. Gong, Phys. Rev. B **74**, 193301 (2006).

[66] P. M. Smith, PhD Thesis, Simon Fraser University (2012).

[67] C. L. Kane and E. J. Mele, Phys. Rev. Lett. **95**, 146802 (2005).

[68] D. Hsieh, D. Qian, L. Wray, Y. Xia, Y. S. Hor, R. J. Cava and M. Z. Hasan, Nature **452**, 970 (2008).

[69] http://www.itp.uni-hannover.de/zawischa/ITP/kalcal.html.

[70] R. Shen, L. B. Shao, B. Wang, and D. Y. Xing, Phys. Rev. B **81**, 041410(R) (2010).

[71] D. Bercioux, D. F. Urban, H. Grabert, and W. Häusler Phys. Rev. A **80**, 063603 (2009).

[72] V. Apaja, M. Hyrkäs, and M. Manninen, Phys. Rev. A **82**, 041402(R) (2010).

[73] B. Seradjeh, C. Weeks, and M. Franz, Phys. Rev. B **77**, 033104 (2008).

[74] I. F. Herbut, Phys. Rev. B **83**, 245445 (2011).

[75] R. Jackiw and C. Rebbi, Phys. Rev. Lett. **36**, 1116 (1976).

[76] B. Roy, P. M. Smith, and M. P. Kennett, Phys. Rev. B **85**, 235119 (2012).

[77] B. Roy, Phys. Rev. B **85**, 165453 (2012).

[78] K. Cheung, PhD Thesis, Simon Fraser University (2012).

[79] C. Weeks and M. Franz, Phys. Rev. B. **82**, 085310 (2010).

[80] K. Kaveh and I. F. Herbut, Phys. Rev. B **71**, 184519 (2005).

[81] K. v. Klitzing, Phys. Rev. Lett. **45**, 494 (1980).

[82] D. C. Tsui, H. L. Stormer, and A. C. Gossard, Phys. Rev. Lett. **48**, 1559 (1982).

[83] T. Shen, J. J. Gu, M. Xu, Y. Q. Wu, M. L. Bolen, M. A. Capano, L. W. Engel, P. D. Ye, App. Phys. Lett. **95**, 172105 (2009).

[84] I. F. Herbut, Phys. Rev. B **66**, 094504 (2002).

[85] P. Hosur, S. Ryu, and A. Vishwanath, Phys. Rev. B **81**, 045120 (2010).